Atmospheric and Surface contributions to Planetary Albedo and their relationship to the total meridional energy transport

Aaron Donohoe* and David S Battisti*

*Department of Atmospheric Sciences, University of Washington, Seattle, Washington

(Manuscript submitted 21 July 2010)

Corresponding author address: Aaron Donohoe, University of Washington, 408 ATG building, box 351640, Seattle, WA, 98195
Email: aaron@atmos.washington.edu

ABSTRACT

The meridional distribution of incident solar radiation and planetary albedo both contribute to the equator-to-pole gradient in absorbed solar radiation (ASR) in the observed climate system. While the former component is determined by the Earth-Sun geometry and composes 60% of the equator-to-pole gradient in ASR, the latter component makes a significant (40%) contribution to the ASR gradient and is potentially a function of climate state due to its dependence on both atmospheric and surface albedo. In turn, the equator-to-pole gradient in planetary albedo is found to be primarily (86% - 89%) dictated by atmospheric albedo with meridional gradients in surface albedo playing a much smaller role in forcing the climate system on the equator-to-pole scale. Simulations of the pre-industrial climate system using the CMIP3 coupled models show large differences in the equator-to-pole gradient in planetary albedo which are mainly due to differences in the simulated cloud distribution, with surface processes playing a much smaller role. The inter-model spread in total meridional heat transport is also primarily due to differences in the simulated cloud distribution. Further model simulations demonstrate that the surface albedo changes associated with moving from the present climate to an ice free climate have a small effect on the equator-to-pole gradient of ASR as compared to the uncertainty in simulated cloud distributions, and hence a small effect on the meridional heat transport.

1. Introduction

The equator-to-pole gradient of absorbed solar radiation (ASR) plays a fundamental role in forcing the Earth's climate system. Orbitally induced changes in the equator-to-pole gradient of ASR force profound changes in the equator-to-pole temperature gradient in climate models (Dong and Valdes 1995; Phillips and Held 1994) and the consequences are recorded in the geological and paleoclimate records (e.g. IMAP 1981). Virtually all atmospheric and oceanic motions derive their energy from meridional gradients in ASR (Hartmann 1994) and there is evidence that the total meridional heat transport in the climate system is tightly constrained by the equator-to-pole gradient in ASR (Enderton and Marshall 2009)[1].

In a seminal paper, Stone (1978) calculated that approximately two thirds of the observed equator-to-pole gradient in ASR is due to the Earth-Sun geometry and the resulting meridional distribution of incident solar radiation at the top of the atmosphere and the remaining one third is due to the equator-to-pole contrast in planetary albedo. Stone emphasized that the latter component was nearly energetically balanced by the equator-to-pole gradient in outgoing longwave radiation (OLR) such that the equator-to-pole gradient in net radiation was determined entirely by the Earth-Sun geometry, although subsequent work by Enderton and Marshall (2009) demonstrated that this result is not supported by modern observations or in climate model simulations. Enderton and Marshall (2009) found that approximately 35% (40%) of the observed equator-to-pole gradient of ASR in the Northern (Southern) Hemisphere is due to the equator-to-pole

[1] There is evidence that this relationship does not hold in very cold climates such as the Snowball Earth where latent heat transport is negligible (Pierrehumbert 2005).

gradient in planetary albedo and that the climate simulated by climate models is extremely sensitive to changes in the equator-to-pole gradient of planetary albedo.

Partitioning of the ASR gradient into components associated with orbital geometry and planetary albedo is useful because, while the former is externally forced, the latter is a strong function of the climate state and thus may provide important feedbacks when external forcing changes. More importantly, while the equator-to-pole gradient in solar insolation varies by approximately 5% over the entire obliquity cycle, there is little *a priori* constraint on the possible range of the meridional gradient in planetary albedo. Thus, a small perturbation in the external forcing may produce a disproportionately large change in the meridional gradient in ASR via changes in the meridional gradient of planetary albedo (i.e. changes in cloud or snow/ice cover) associated with the *response* of the climate system. Hence, an assessment of the sources that contribute to the meridional gradient in planetary albedo is essential for understanding how and why the meridional gradient in forcing (i.e. the meridional gradient of ASR) will change in response to a perturbation in the external forcing.

More specifically, planetary albedo is a function of the optical properties of objects within the atmosphere (such as clouds, water vapor, and aerosols) and objects that constitute the planet's surface (such as ice, ocean, and trees) (Wielicki et al. 1995). It is convenient to discuss the atmosphere's influence on planetary albedo in three bulk processes: (a) clouds that directly reflect incident solar radiation back to space, (b) atmospheric opacity (due to reflection and absorption in the atmosphere) that limits the amount of downwelling solar radiation reaching the surface and thus can be reflected upward by the surface albedo and, (c) atmospheric opacity of solar radiation upwelling

from the surface that limits the amount of radiation reflected by the surface that escapes to space (Qu and Hall 2005). Thus, the atmosphere influences the planetary albedo by

y of direct reflection back to space (process a) and by attenuating the effect of surface albedo on planetary albedo (processes b and c). Both the atmospheric and surface contributions to planetary albedo are functions of the climate state.

Several studies have analyzed the surface contribution to local planetary (i.e. top of the atmosphere) albedo in the polar regions. Gorodetskaya et al. (2006) found that changing ice/snow concentrations from 0% to 100% resulted in local planetary albedo changes of order 0.20 with some regional dependence. Assuming the change in surface

edo associated with transitioning from a completely snow/ice free surface to a completely snow/ice covered surface is of order 0.5, this result suggests that the atmosphere attenuates the surface albedo change's influence on planetary albedo by approximately 60%. Qu and Hall (2005) found that surface reflection accounts for less than 25% of the local planetary albedo in the ice- and snow-covered regions of the planet and the remainder is due to clouds. They also found that, while the year-to-year variability of planetary albedo in cryospheric regions was dominated by changes in surface albedo, atmospheric processes attenuated the contribution of surface albedo changes to planetary albedo changes by as much as 90%.

The Earth has a pronounced equator-to-pole gradient in surface albedo due to latitudinal gradients in the fraction of area covered by ocean and land, the latitudinal gradients in land vegetation, and the spatial distribution of land and sea ice (Robock 1980). The contribution of the equator-to-pole gradient in surface albedo to the equator-to-pole gradient in planetary albedo is still an unresolved question in climate dynamics,

however, because there is considerable attenuation of the surface albedo by the atmosphere. While simplified energy balance models (EBMs) have often assumed that the meridional gradient in planetary albedo scales as the meridional gradient in surface albedo (i.e. Budyko 1969 and North 1975), this assumption is unwarranted due to the atmosphere's influence on planetary albedo; the step function change of planetary albedo at the ice-age specified by EBMs is inconsistent with the observed meridional structure of planetary albedo (Warren and Schneider 1979) and more recent parameterizations of planetary albedo in EBMs have suggested that the atmosphere damps the influence of surface albedo changes on the top of atmosphere (TOA) radiative budget (Graves et al. 1993).

In this study, we quantify the relative contributions of Earth-Sun geometry and planetary albedo to the observed distribution of ASR and quantify the relative contributions of atmospheric and surface processes to the observed planetary albedo – and hence to the observed equator-to-pole gradient in ASR (Section 2). We then perform the same analyses on the output of the pre-industrial integrations from the climate models used in the International Panel on Climate Change (IPCC) Fourth Assessment Report (AR4) to determine whether the meridional gradient in planetary albedo and its attribution to surface and atmospheric processes seen in the observations is captured in the model simulations. We also calculate the inter-model spread in the equator-to-pole gradient of ASR and determine whether this spread is due to differences in atmospheric processes or to differences in surface processes (Section 3). Next, we discuss the implications of the inter-model spread in the equator-to-pole gradient of ASR for the total heat transport simulated in the climate system (Section 4). Finally, we analyze the

hemispheric average and meridional gradients of planetary albedo in vastly different climate states with altered surface albedo distributions ranging from the last glacial maximum to an ice-free aquaplanet (Section 5). A discussion of the implications of our results for altered climate states follows.

2. Observed partitioning of planetary albedo

In this section, we partition the observed meridional gradient of ASR into two components: a component due to the Earth-sun geometry, and a component due to the meridional gradient in planetary albedo. We then partition the observed planetary albedo into atmospheric and surface components and assess the contribution of each component to the ASR gradient.

We use the TOA shortwave radiation data from the Earth Radiation Budget periment (ERBE) climatology (Barkstrom et al. 1989). The surface shortwave flux is from the CERES "AVG" fields which are derived by assimilating the satellite observations into a radiative transfer model to infer the surface fluxes (Rutan et al. 2001). All data discussed in this study are annual, solar weighted (over the seasonal cycle) averages.

a. Contribution of geometry and planetary albedo to the ASR gradient

e divide the globe into three regions: the region that absorbs a surplus of solar radiation relative to the global average (defined as the tropics) and the region of each hemisphere that absorbs a deficit of solar radiation relative to the global average (defined as the extratropics). As an index of the equator-to-pole gradient in ASR, we calculate the

spatial integral of the ASR anomalies (defined as the deviation from the global average) over the extratropical regions in each hemisphere (a quantity we denote as ASR*, illustrated in Figure 1a):

$$ASR^* = -2\pi R^2 \int_{x(ASR'=0)}^{1} ASR' \, dx \ , \qquad (1)$$

where x is the sine of latitude (x=1 is the north pole), R is the Earth's radius, ASR' is the zonally averaged ASR anomaly[2]. The negative sign is chosen so that the ASR deficit over the extratropics defines ASR^* as a positive number. Equation (1) is the ASR deficit (ASR^*) in the Northern Hemisphere (NH) extratropics; a similar expression with modified limits of integration holds for the Southern Hemisphere (SH). By definition, the sum of ASR^* in the two hemispheres is equal to the ASR surplus (relative to the global average) integrated over the tropics. Therefore, this quantity represents the difference in energy absorbed in the tropics and in the extratropics. In a steady climate system, the global averaged ASR is balanced by the outgoing longwave radiation (OLR) at the TOA. Therefore, ASR^* in each hemisphere must be equal to the sum of the OLR anomaly integrated over the extratropics and (atmospheric and oceanic) heat transport from the tropics to the extratropics.

That ASR^* is non-zero is due to both the meridional gradient in incident solar radiation and to the meridional gradient in the planetary albedo. We can partition ASR^*

[2] Throughout this work, anomaly is defined as the difference between a quantity and the global average of that quantity.

into these two component contributions by writing the planetary albedo and incident solar radiation as the sum of a global mean and a spatial anomaly:

$$ASR(x) = a(x)\ \ S(x) = (\overline{a} + a'(x))\ \ (\overline{S} + S'(x)) = \overline{a}\,\overline{S} + \overline{a}S'(x) + a'(x)\overline{S} + a'(x)S'(x) \quad (2)$$

where *a(x)* is the co-albedo (one minus albedo), overbars denote a spatial average, and primes indicate spatial anomalies[3]. *ASR** can be calculated from equation 2 by subtracting the global mean of each term and integrating over the extratropics:

$$ASR* = -2\pi R^2 \left[\overline{a} \int_{x(ASR'=0)}^{1} S'(x)\ dx \quad + \overline{S} \int_{x(ASR'=0)}^{1} a'(x)\ dx \quad + \int_{x(ASR'=0)}^{1} \left[S'(x)a'(x) - \frac{1}{2}\int_{-1}^{1} S'(x)a'(x)dx \right] dx \right] \quad (3)$$

[3] An alternative approach to dividing the fields into a global mean and spatial anomaly is to expand the variables in terms of even Legendre polynomials in each hemisphere, as was done in Lorenz (1978) and Enderton and Marshall (2009). Our *ASR** and component contributions to *ASR** are proportional to the second Legendre coefficients provided that the spatial structure of ASR projects entirely onto the zeroth and second Legendre polynomials. The total ASR contrast calculated by these two methods agree to within 2%; the first order terms agree to within 5% of each other, and the second order term (the covariance) agrees to within 30%. The discrepancy is larger for the second order term because, even if the planetary albedo and incident solar radiation were fully captured by the first two Legendre polynomials, the covariance projects primarily on the 4th Legendre polynomial and only secondarily onto the 2nd polynomial (i.e. note the spatial structure of the covariance term in Figure 1B). In this regard, our index of the meridional difference is more accurate than that obtained by expansion in terms of Legendre polynomials, although the primary conclusions reached here are independent of the methodology employed.

The first term on the right hand side of Equation 3 represents the equator-to-pole difference in incident solar radiation modified by the global average coalbedo and is primarily a function of the Earth-Sun geometry; it is the equator-to-pole contrast of ASR that would exist if there were no meridional variations in planetary albedo. The second term is the contribution of the meridional gradient in planetary albedo to *ASR** in the absence of spatial variations of incident solar radiation (Figure 1b). The last term is the covariance of the spatial anomalies in planetary albedo and incident radiation. The covariance contributes to a positive global mean ASR (the second term within the integrand) because the high latitude regions receive a deficit of incident solar radiation and have an anomalously high planetary albedo such that the global average planetary coalbedo ($\overline{a}$) is smaller than the global mean solar weighted planetary coalbedo. Similarly, the last term in Equation 3 makes a negative contribution to *ASR** because the high planetary albedo regions receive less incident radiation than the global average value that appears in the second term of Equation 3 such that the contribution to *ASR** due to the meridional gradient in planetary albedo is overestimated by the second term alone. Therefore, we can interpret the covariance term as a correction to the planetary albedo's contribution to *ASR**.

Equation 3 divides *ASR** into a geometric component that exists in the absence of any meridional gradient in planetary albedo (the first term, red line in Figure 1b,c) and a component that owes its existence to the meridional gradient in albedo (the sum of the

second and third terms, Figure 1c). Hence, in the remainder of this study, we will define *the planetary albedo's contribution to ASR** to be the sum of the second and third terms[4].

The equator-to-pole contrast in ASR, *ASR** (Equation 1), is 8.1 PW (8.7 PW) in the NH (SH). Integration of the terms in Equation 3 finds that spatial variations in planetary albedo contribute 2.9 PW (3.5 PW) to *ASR**, representing 35% (41%) of the total equator-to-pole forcing of the NH (SH).

b. Partitioning planetary albedo into atmospheric and surface components

1. METHODOLOGY

We now describe a methodology for partitioning the planetary albedo into atmospheric and surface components, given the upwelling and downwelling solar fluxes at both the TOA and the surface. A similar methodology was described by Taylor et al. (2007)[5]. At each gridpoint we build a single layer model of solar radiation that accounts for three shortwave processes: atmospheric reflection, atmospheric absorption and,

[4] It is equally valid to interpret Equation 3 as consisting of a component that exists in the absence of a meridional gradient in solar insolation (second term) and a component owing its existence to the meridional gradient of solar insolation (the sum of the first and third term). The interpretation is contingent on the phrasing of the question. In this regard, the grouping of the terms we adopt in this paper is a lower limit assessment of the planetary albedo gradient's contribution to *ASR**.

[5] Taylor et al. (2007) partitioned the planetary albedo feedback between atmospheric and surface processes using the identical conceptual model described here except that they assumed atmospheric absorption of shortwave radiation only occurred during the first downward pass through the atmosphere. We elect to account for atmospheric absorption of the shortwave radiation reflected by the surface because calculations using a radiative transfer model (Kato et al. 1999) simulations show increased atmospheric absorption of solar radiation as the surface albedo is increased from 0 to 1, indicating that solar radiation in the atmospheric absorption bands are *not* depleted in a single pass through the atmosphere.

surface reflection. We assume that each of these processes is isotropic and absorbs/reflects a fixed percent of the existing solar radiation per pass through the atmosphere/interaction with the surface. For example, a percentage of the downwelling solar radiation incident at the TOA (S) is reflected by the atmosphere (R), a percentage is absorbed by the atmosphere (A) and the remainder is transmitted to the surface. Of the transmitted radiation, a portion is reflected at the surface (the surface albedo, α) back toward the atmosphere. Of this reflected radiation, a portion R is reflected back to the surface by the atmosphere, a portion A is absorbed within the atmosphere, and the remainder is transmitted to space (Figure 2). These processes can be repeated for an infinite number of reflections. For example, the annual mean upwelling solar flux at each gridpoint at the TOA can be expressed as:

$$F\uparrow_{TOA} = S[R + \alpha(1-R-A)^2 + \alpha^2 R(1-R-A)^2 + \alpha^3 R^2(1-R-A)^2 .....$$
$$= SR + S\alpha(1-R-A)^2[1 + (\alpha R) + (\alpha R)^2 ....] = SR + S\alpha\frac{(1-R-A)^2}{1-\alpha R} \quad , \qquad (4)$$

where $F\uparrow_{TOA}$ is the upwelling solar flux at the TOA and the convergence of the infinite series to the final expression on the right hand side is required because both R and α are less than 1 (Qu and Hall 2005). Similar convergent infinite series can be obtained for the downwelling and upwelling solar fluxes at the surface, each expressed in terms of R, A, and α.

Our theoretical model (Figure 2) gives expressions for the upwelling and downwelling solar fluxes at the TOA and the surface (4 equations) as a non-linear function of four unknown variables: S, R, A and, α. Therefore, given the observations of upwelling and downwelling solar radiation at the TOA and at the surface at each gridpoint, the system can be solved for the unknown variables. In practice, the

downwelling radiation at the TOA determines S and the ratio of upwelling to downwelling radiation at the surface determines α such that the system can be reduced to two equations (Equation 4 and a similar expression for downwelling radiation at the surface) and two unknowns (A and R)[6].

Solving the system results in spatial maps of R (Figure 3D) and A (not shown). We can then partition the upwelling radiation at the TOA into atmospheric and surface components; the atmospheric component is due to direct reflection by the atmosphere (the first term on the right hand side of Equation 4) and all the solar radiation that is reflected by the surface and eventually passes through the TOA (the second term on the right hand side of Equation 4) is attributed to the surface contribution to planetary albedo. Dividing these terms by S results in the atmospheric contribution to planetary albedo, R, and the surface contribution to planetary albedo, $\frac{\alpha(1-R-A)^2}{1-\alpha R}$. These components are shown in Figure 3, expressed as a percent of the incident solar radiation at the TOA that is reflected back to space.

2. RESULTS

The maps of surface and planetary albedo exhibit large values in the polar regions and relatively small differences in the zonal direction (Figure 3); the predominant spatial structure in both maps is an equator-to-pole gradient. However, the largest meridional

[6] One can show that all possible solutions to our equations have $0 \leq R \leq 1$ and $0 \leq A \leq 1$, although it is not clear to us whether a solution to the generalized system of equations must exist. Nonetheless, solutions to the system (to within numerical precision) exists for all gridpoints and datasets and GCM output discussed in this manuscript. Furthermore, all solutions (A and R values at each gridpoint) discussed here are unique.

gradient of the surface albedo occurs at the transition to the cryospheric regions (around 70˚ in each hemisphere) whereas the meridional gradient in planetary albedo is spread across the storm track regions (from 30˚ to 60˚).

The percentage of solar radiation absorbed during a single pass through the atmosphere (not shown) also features a predominant equator-to-pole gradient with tropical values of order 25% and high latitude values of order 15% with still smaller values occurring over topography. The global pattern of atmospheric solar absorption is virtually identical to the pattern of vertically integrated specific humidity (from NCEP reanalysis) with a spatial correlation coefficient of 0.94; this is expected because the atmospheric absorption of solar radiation is predominantly due to water vapor and ozone (Chou and Lee 1996).

The map of the atmospheric contribution to planetary albedo shows several anticipated features: 1. high values of atmospheric reflectance associated with the intertropical convergence zone in the equatorial Pacific; 2. low values in the drier subtropics; 3. high values in the NH Atlantic and Pacific storm tracks and the nearly zonally symmetric SH storm track associated with synoptic storms; 4. high values in the Arctic and West Antarctica that tend to be cloudy during the local summer (Curry et al. 1996); 5. high values over South East Asia associated with extensive cold season stratocumulus (Hahn and Warren 2003).

As is true for the planetary albedo and the atmospheric contribution to the planetary albedo, the surface contribution to planetary albedo is greater in the polar regions than in the tropics. More important, however, is that the surface contribution to the planetary albedo is greatly attenuated by the atmosphere (cf the top two panels of

Figure 3) – so much so that almost everywhere the planetary albedo is largely determined by the atmospheric and not the surface contribution (cf the right two panels of Figure 3). Our simple radiative model predicts that the surface contribution to planetary albedo will be attenuated by square of the atmospheric transmissivity: $(1-R-A)^2$ (Equation 4 and Figure 2). In this framework, we can see that while the atmospheric opacity primarily acts to damp the impact of the surface albedo on planetary albedo, the atmosphere also imparts some spatial structure into the map of the surface albedo's contribution to planetary albedo by virtue of the spatial structure in atmospheric opacity. For example, while the surface albedo over Antarctica is fairly spatially uniform, the surface albedo makes a larger contribution to the planetary albedo over East Antarctica because the atmosphere is less opaque (both less cloud and less absorption by water vapor) as compared to West Antarctica.

Atmospheric processes play a much greater role than surface processes in determining the amplitude and structure of planetary albedo, both regionally and in the global average. The (solar weighted) global average planetary albedo of 0.313 is composed of a 0.277 (88% of the total) contribution from atmospheric processes and a 0.036 (12%) contribution from surface processes (Table 1). This global average value is in qualitative agreement with Qu and Hall's (2005) conclusion that, "the atmosphere accounts for much more of the climatological planetary albedo (≥ 75%) than the surface …". The hemispheric average planetary albedo is very similar in both hemispheres (0.3141 in the NH versus 0.3128 in the SH) although the partitioning between atmospheric and surface processes differs slightly between the hemispheres (atmospheric

processes contribute 87.5% of the hemispheric average in the NH as compared to 89.7% in the SH).

The zonal average planetary albedo, partitioned into atmospheric and surface components, is shown in Figure 4a. With the exceptions of the cryosphere regions, the meridional structure of planetary albedo is almost entirely due to the meridional structure in cloud reflection; both the meridional structure of cloud fraction and solar zenith angle (Minnet 1999) contribute to the meridional structure of atmospheric albedo.

We define the surface's contribution to planetary albedo to be the "effective" surface albedo; it represents the percent of incident solar radiation that is reflected at the surface that makes it back out to space:

$$\text{"effective" surface albedo} = \frac{\alpha(1 - R - A)^2}{1 - \alpha R} \quad . \qquad (5)$$

As can be seen in Figure 4b (or by comparing the top two panels of Figure 3), the "effective" surface albedo is much smaller than the actual surface albedo because (1) the downwelling solar radiation at the TOA is attenuated by atmospheric reflection and absorption as it passes downward through the atmosphere and (2) the solar radiation reflected by the surface is attenuated by atmospheric absorption and reflection as it passes upwards from the surface to the TOA. Even over the polar regions, where the zonal mean surface albedo exceeds 70%, the "effective" surface albedo never exceeds 30%. If we define the atmospheric attenuation of surface albedo as one minus the ratio of the "effective" surface albedo to the actual surface albedo (Figure 4c), then the atmospheric attenuation of the surface albedo ranges from a maximum of 80-85% in the storms tracks to a minimum of 60% in the dry subtropics. The meridional structure of attenuation is less important in limiting the contribution of surface albedo to ASR^* than is the global

average value of attenuation which suggests that the atmospheric opacity limits the surface's contribution to planetary albedo throughout the globe and, therefore, also damps the equator-to-pole gradient in the surface albedo's contribution to the equator-to-pole planetary albedo gradient. This is partly because solar radiation is attenuated by clear sky processes (i.e. solar atmospheric absorption) which can contribute as much as 50% of the atmospheric attenuation in the global mean (Bony et al. 2006).

Given the surface and atmospheric contributions to planetary albedo (Figure 4a), we now ask: how do surface and atmospheric processes each contribute to *ASR*?* The contribution of atmospheric and "effective" surface albedo to *ASR** can be assessed by first dividing the planetary coalbedo into separate atmospheric and surface components, each with a global mean and spatial anomaly:

$$A(x) = (1 - \alpha_{ATMS} - \alpha_{SURF}) = (1 - \overline{\alpha}_{ATMS} - \overline{\alpha}_{SURF} - \alpha'_{ATMS} - \alpha'_{SURF}) \quad , \tag{6}$$

where the *ATMS* and *SURF* subscripts refer to the atmospheric and surface contribution to planetary albedo. Substituting Equation 6 into the definition of *ASR** in Equation 3 yields the contribution of the atmospheric component of planetary albedo to ASR*:

$$ASR*_{\alpha,ATMS} = 2\pi R^2 \overline{S} \int_{x(ASR'=0)}^{1} \alpha'_{ATMS} dx \; + \; 2\pi R^2 \int_{x(ASR'=0)}^{1} \left[\alpha'_{ATMS} S' \; - \frac{1}{2} \int_{-1}^{1} \alpha'_{ATMS} S' dx \right] dx \quad , \tag{7}$$

where we have again grouped the linear and covariance term together to calculate the total contribution of spatial structure in α_{ATMS} to *ASR**. A similar expression is used to calculate the "effective" surface albedo contribution to *ASR**. The atmospheric planetary

albedo is found to contribute 2.5 PW (3.1) PW to *ASR** in the NH (SH) while the surface is found to contribute 0.4 PW (0.4 PW) to *ASR** (Table 2). These results suggest that, even if the equator-to-pole gradient in surface albedo were to greatly diminish (e.g., in an -free world) the equator-to-pole scale climate forcing would decrease by less than 5% in each hemisphere.

In summary, atmospheric processes were found to be the dominant (88%) contributor to global average planetary albedo while surface processes make a much smaller contribution to the global average planetary albedo. The equator to pole contrast of ASR is composed of an approximately 2/3 contribution from the Earth-Sun Geometry and a 1/3 contribution from the meridional gradient of planetary albedo. The latter component was found to be primarily (approximately 85%) controlled by atmospheric processes, with surface processes playing a much smaller role.

3. Partitioning of planetary albedo and its contribution to ASR* in the climate models used in IPCC AR4

In this Section, we look at the inter-model variability of *ASR** in pre-industrial (PI) simulations of the climate system performed using the climate models that were used in the IPCC AR4. We then employ the same methodology introduced in Section 2 to partition planetary albedo and *ASR** in each model into its atmospheric and surface components. We find, not surprisingly, that the inter-model spread in *ASR** is due to the differences in atmospheric processes and only weakly related to differences in surface albedo.

a. Model runs utilized

The World Climate Research Program (WCRP) maintains an archive of model output from the Climate Model Intercomparison Project 3 (CMIP3), a suite of standardized coupled simulations from 25 global climate models that were included in the International Panel on Climate Change's Fourth Assessment Report (https://esgcet.llnl.gov:8443/index.jsp). The set of model simulations is commonly referred to as the WCRP's CMIP3 multi-model dataset (Meehl et al. 2007). We use the pre-industrial (PI) simulations from the 15 coupled models that provided the output fields required for the analysis presented in this study (Table 3). Each PI simulation is forced with temporally invariant external forcing (CO_2 is set to 280 ppm) and, in principle, represents an equilibrium climate that is in energy balance. In practice, both the global average and the local energy budgets are not balanced in the simulated climatologies (Lucarina and Ragone 2010); hence, we make corrections to balance the global annual mean radiative budget by adding a spatially and temporally invariant constant to the OLR field, prior to performing the analysis[7].

b. Results

1. ALBEDO AND PLANETARY ALBEDO

Averaged over all the CMIP3 models, the global average planetary albedo is 0.3036, which is biased low relative to the observed value of 13 (Table 1). The inter-

[7] The only calculated field discussed here that is affected by this correction is the IT that is discussed in the next section; this correction ensures the global mean heat transport divergence is zero and the resulting MHT is independent of whether the heat transport divergence is integrated from the South Pole to the North Pole or vice versa.

model spread (two standard deviations) in planetary albedo is 0.016 corresponding to a TOA net shortwave difference of approximately 5.5 Wm^{-2} across the models. Averaged across the models, atmospheric processes contribute 87% of the global average planetary albedo which agrees with the observed partitioning of global average planetary albedo between atmospheric and surface processes.

As is true of the observations, the two hemispheres contribute nearly equally to the global average planetary albedo in the models (spread on the y-axis of Figure 5). Also in agreement with the observations, surface processes contribute slightly more to the hemispheric average planetary albedo in the NH than in the SH (the offset on the x-axis of Figure 5b between the NH and SH data).

The inter-model spread in the atmospheric contribution to hemispheric average planetary albedo (2σ=0.022) is much greater than that of the surface albedo (2σ=0.012). Overall, the inter-model spread of hemispheric average planetary albedo is well correlated with the inter-model spread in the atmospheric contribution to planetary albedo (Figure 5a, R^2 = 0.53 and 0.71 in the NH and SH) and is poorly correlated with the surface contribution to planetary albedo (Figure 5b). The global average planetary albedo is poorly correlated with the surface albedo contribution to planetary albedo because (1) the surface contribution to hemispheric average planetary albedo is small compared to the atmospheric contribution and (2) the inter-model spread in surface contribution to hemispheric average planetary albedo and surface contribution to hemispheric average planetary albedo are anti-correlated (not shown). The anti-correlation between the surface and atmospheric contribution to planetary albedo is expected because an atmosphere that reflects solar radiation also has a reduced solar transmissivity and therefore attenuates the

"effective" surface albedo as seen from the TOA (Equation 5) relative to a less reflective atmosphere. This point is further discussed in the next subsection.

The inter-model spread in global and hemispheric average planetary albedo is primarily determined by atmospheric processes as opposed to surface albedo for three reasons: (1) the climatological planetary albedo is primarily (87%) determined by atmospheric reflection; (2) the surface albedo contribution to planetary albedo is strongly attenuated by the atmospheric opacity; and (3) a portion of the inter-model spread in surface albedo is a consequence of the inter-model spread in atmospheric opacity. As a consequence, the hemispheric average *surface albedo* is very weakly correlated with hemispheric average planetary albedo (Figure 6).

The spatial map of the multi-model average planetary albedo is very similar to

t observed with the exception that the models are biased low (the observations are more than two standard deviations above from the multi-model mean) in Saharan Africa, the Arabian Peninsula, and the subtropical stratocumulus regions (not shown). The zonal average surface albedo, planetary albedo and the surface and atmospheric contributions to planetary albedo for each member of the CMIP3 PI ensemble are co-plotted (dashed black lines) in Figure 7a-d alongside the observations (light blue lines). (Results from some additional model experiments are also shown in Figure 7 and will be discussed in Section 5.) Overall, the meridional structure of surface albedo is consistent with the observations, though there are some large regional differences between the observations and models[8]. The zonal average planetary albedo (Figure 7b) exhibits substantial inter-

[8] For example, two of the models (MRI and INMCM3) have anomalously large tropical surface albedo relative to the other models; in both cases, this is a result of a relatively

model spread, exceeding 0.1 units (2σ) in the mid and high latitudes (Figure 8). The inter-model spread is primarily associated with the mid-latitude storm track regions over the North Atlantic, North Pacific, and Southern Ocean.

In agreement with the observations, the atmospheric contribution to planetary albedo in the CMIP3 ensemble is larger than the surface contribution to planetary albedo at all latitudes with the exception of the high Arctic and Antarctic (c.f. the bottom two panels of Figure 7) . The inter-model spread in the meridional structure of planetary albedo, as measured by the standard deviation of the atmospheric and surface contribution to planetary albedo, is largely due to differences in the atmospheric contribution to planetary albedo except in the high polar regions where surface and atmospheric processes contribute comparably to the inter-model spread in planetary albedo (Figure 8). This result suggests that model differences in the meridional structure

---

large ocean albedo relative to the other models. The largest model spread in the surface albedo, however, is in the cryospheric regions; in the polar regions, the surface albedo in the CSIRO model is extremely low (greater than two standard deviations below the inter-model mean albedo) while that for the ECHAM model is large. The IAP model has a large surface albedo (exceeding the inter-model average by greater than two standard deviations) in the mid-latitudes (between 50˚ and 65˚) of both hemispheres due to the known equatorward model bias in the sea ice edge (Zhou et al. 2008). It is beyond the scope of the present work to assess whether the large differences in the surface albedo in the polar regions of the models are due to differences in the latitudinal extent of the cryosphere or to differences in the values of albedo assigned to ice and snow covered surfaces.

of planetary albedo are primarily determined by atmospheric (cloud) processes and only weakly by inter-model differences in surface processes.

With the exception of the SH ice margin, the inter-model standard deviation of the atmospheric contribution to planetary albedo exceeds the total inter-model standard deviation of planetary albedo (Figure 8); this result is a consequence of the negative correlation between the atmospheric contribution to planetary albedo and the surface contribution to planetary albedo (not shown) that was also noted in the hemispheric averages in the previous section. The latter negative correlation is expected based on our solar radiation model (i.e. the "effective" surface albedo's negative dependence on atmospheric reflectance, R, in the second term on the right hand side of Equation 4) ; if two models had identical surface albedo in the Arctic but different cloud reflectance (and hence atmospheric transmissivities) the model with the larger atmospheric reflectance would have a reduced "effective" surface albedo because the reflective surface is less visible from the TOA. This result is interesting because it suggests that a portion of the inter-model spread in "effective" surface albedo is due to atmospheric variability across models as opposed to the inter-model spread of surface albedo. A quantitative assessment of these two effects is beyond the scope of the present work.

2. *ASR** AND ITS COMPONENTS IN THE PI SIMULATIONS USING THE CMIP3 MODELS

We now examine the hemispheric gradient in ASR, *ASR**, and its decomposition into atmospheric and surface components in the PI simulations from the CMIP3 models.

We only consider the planetary albedo contribution to *ASR** in this discussion because the meridional gradient of incident radiation does not vary between runs[9].

In the ensemble average, the CMIP3 models reproduce the observed *ASR** (see Table 2). The multi-model averaged *ASR**in the NH (SH) is PW (8.4 PW), while that observed is 8.1PW (8.7PW). The breakdown of *ASR** into atmospheric and surface components is also well reproduced by the multi-model average: in the NH (SH), the CMIP3 average atmospheric contribution to *ASR** is 2.4PW (2.9PW), while that observed is 2.5PW (3.1PW); in the NH (SH), the CMIP3 average surface contribution to *ASR** is 0.5PW (0.3PW), while that observed is 0.4PW (0.4PW).

Figure 9 shows a scatter plot of the total *ASR** against (a) the atmospheric and (b) surface contributions to *ASR** from the CMIP3 models (plus signs) in the northern (blue) and southern (red) hemispheres. Although the multi-model averaged *ASR** (and its components) compared favorably to the observed *ASR*,* there is a remarkably large range in the simulated *ASR** (2 sigma = 0.9PW and 1.2PW in NH and SH). Almost all of the inter-model spread in *ASR** is due to the atmosphere. The atmospheric contribution to *ASR** (2ma = 1.2PW and 1.4PW in the NH and SH) is highly correlated with the total atmospheric contribution to *ASR** ($R^2 = 0.94$), and the best-fit slope in each hemisphere is nearly unity. In comparison, the inter-model spread in the surface contribution to *ASR** is small (2σ = 0.5PW and 0.4PW in the NH and SH, respectively) and not correlated with total *ASR**.

[9] Technically, even though the orbital parameters in all PI runs are equal, the incident contribution to *ASR** does vary due to the dependence on $\bar{a}$. In practice, the inter-model variability in this contribution is smaller than 1% of the incident solar radiation's contribution to *ASR**.

We can take two limiting models for how the meridional structure of atmospheric and surface reflection contribute to *ASR**: "Model A" in which the surface albedo is spatially invariant so that *ASR** is determined entirely by the spatial structure of atmospheric reflection and "Model B" in which the atmosphere is transparent to shortwave radiation so that *ASR** is determined entirely by the surface albedo gradient. In the case of "Model A", *ASR** would equal the sum of the atmospheric contribution to *ASR** (calculated via Equation 7) and the incident (geometric) component of 5.2PW (black line, Figure 9a). "Model A" is an excellent fit to the inter-model spread in *ASR**. "Model A" slightly under predicts *ASR** in all cases because the "effective" surface albedo always makes a positive contribution to *ASR**; the vertical offset between the black line and the individual model results in Figure 9a is the surface contribution to *ASR**. This suggests that, while surface processes do play a role in determining *ASR**, the majority of the inter-model spread in *ASR** (94%) is explained by differences in atmospheric reflection.

At the other end of the spectrum, if the atmosphere were indeed transparent ("Model B"), *ASR** would be equal to the incident (geometric) contribution plus the surface reflection contribution given by the global average solar insolation times the surface albedo anomaly integrated over the extratropics plus a second order term:

$$SURF^* = \bar{S} \int_{x(ASR'=0)}^{1} \alpha' \, dx + \int_{x(ASR'=0)}^{1} \left[\alpha' S' - \frac{1}{2} \int_{-1}^{1} \alpha' S' \, dx \right] dx \quad , \tag{8}$$

where α' is the surface albedo anomaly from the global average. *SURF** is the contribution of the surface albedo to *ASR** if the atmosphere is transparent to shortwave

radiation. The theoretical prediction of "Model B" is co-plotted with the CMIP3 PI simulations in Figure 10; "Model B" is clearly a poor description of the CMIP3 ensemble. Surface albedo plays a negligible role in determining the inter-model differences in *ASR** because the surface albedo is strongly attenuated by the atmosphere and the inter-model spread in atmospheric reflection overwhelms the surface albedo contribution to planetary albedo spread.

Collectively, these results suggests that differences in atmospheric reflection are, by far, the primary reason for the remarkable spread in *ASR** in the CMIP3 ensemble of PI simulations.

4. ASR*, total Meridional Heat Transport, and the equator-to-pole temperature gradient in the CMIP3 models

In this section, we examine the relationship between *ASR**, the maximum total meridional heat transport (MHT), and the surface temperature gradient in the CMIP3 models. We find that the maximum total meridional heat transport is strongly related to the atmospheric component of *ASR** (and to the total *ASR**) and not related to the surface contribution to *ASR** (hence, not to the surface albedo).

We use the same definitions and methods outlined in Section 2 to calculate *ASR** and the component contributions to *ASR**. For each model, we determine the total (atmosphere plus ocean) zonally averaged MHT to the extratropics of each hemisphere by noting that, in an equilibrium climate, the net radiative deficit spatially integrated from latitude to the pole is exactly balanced by MHT into the region poleward of (Trenberth and Caron 2001):

$$MHT(\theta) = -2\pi R^2 \int_{x=\sin(\theta)}^{1} \left[ASR(x) - OLR(x) \right] dx \quad , \tag{9}$$

where OLR is the zonally averaged outgoing longwave radiation. If we set the limit of integration to $=sin(\ _m)$, where $_m$ is the latitude where the zonally averaged ASR and OLR are equal, then Equation 9 yields the maximum zonally averaged meridional heat transport. If x_m also closely coincides with the latitude at which ASR' = 0, then we can approximate the maximum $MHT(x_m)$ in terms of ASR^* and an analogous quantity, OLR^*:

$$MHT(x_m) = -2\pi R^2 \int_{x=x_m}^{1} \left[ASR(x) - OLR(x) \right] dx \cong ASR^* - OLR^* \quad , \tag{10}$$

where OLR^* is defined as

$$OLR^* = -2\pi R^2 \int_{x(OLR'=0)}^{1} OLR'(x) dx \quad , \tag{11}$$

where OLR' is the OLR anomaly from the global mean and the negative sign ensures OLR^* is positive. The near equality in Equation 11 holds exactly if the meridional nodes of the OLR' and ASR' are co-located; in all calculations presented here the near equality holds to within 1% of the MHT in all simulations (the average error in the approximation is 0.3%). In this framework, the spatially integrated deficit in ASR in the extratropics (ASR^*) must be balanced by either heat transported from the tropics to the extratropics or by anomalously low OLR in the extratropics (OLR^*). As an example, in the observed climate system, the annual mean ASR^* in the NH extratropics is 8.1 PW and is balanced by an OLR^* of 2.4 PW and a peak meridional heat import of 5.7 PW; in the SH extratropics, an ASR^* of 8.7 PW is balanced by 3.2PW OLR^* and 5.5 PW of MHT.

As indicated from Equation 10, the equator-to-pole gradient in absorbed solar radiation, ASR*, forces a circulation that is intimately linked to the total meridional heat transport, MHT. Lucarini and Ragone (2010) showed that climate models generally agree on the meridional structure of MHT, but the peak amplitude of MHT varies across the CMIP3 models by as much as 20%. In the context of our theoretical framework (Equation 10), we expect that the differences in the peak MHT simulated by the models will be due to differences in the simulated *ASR**, *OLR** or, some combination of the two. Looking across models, there is no correlation between peak MHT and *OLR** simulated by the models (not shown). In contrast, the simulated peak MHT is highly correlated with *ASR** ($R^2 = 0.67$ in the NH; 0.74 in the SH). The tight relationship between *ASR** and peak MHT is almost entirely due to differences across models in the atmospheric contribution to planetary albedo (Figure 11a); 72% (81%) of the variance in the inter-model spread of the peak MHT in the NH (SH) is explained by the inter-model spread in the atmospheric contribution to *ASR**, while the correlation of peak MHT with the surface contribution to *ASR** is indistinguishable from zero. This result suggests that the differences in peak total meridional heat transport simulated by the models are primarily due to the differences in the optical properties of the atmosphere (clouds reflection and atmospheric absorption) and not due to differences in the dynamical or longwave radiative processes across the models[10].

[10] From an energetics perspective, the linear best fit of the simulated peak MHT in the NH is positively offset from the linear best fit of peak MHT in the SH because *OLR** is larger (by an average of 0.7 PW) in the SH due to the cold Antarctic continent radiating anomalously low OLR . From a dynamics perspective, the positive NH MHT offset is

We define an index of the equator-to-pole temperature gradient (*TS**) as the spatial average of the surface temperature anomaly from the global mean over the extratropical regions:

$$TS^* = \frac{\int_{x(ASR'=0)}^{1} TS'(x)dx}{\int_{x(ASR'=0)}^{1} dx}, \quad (9)$$

where TS' is the departure of the surface temperature from the global average value. Although the peak MHT is highly correlated with *ASR** across the models, there is no consistent relationship between the simulated equator-to-pole gradient in surface temperature (*TS**) and *ASR**-- in either hemisphere (Figure 11b). This result is surprising, since *ASR** is very well correlated with the equator-to-pole gradient of absorbed solar radiation at the surface (not shown, $R^2 = 0.95$). This suggests that local processes governing the surface energy budget (i.e. boundary layer processes and turbulent energy fluxes) are more important than *ASR** for explaining the inter-model spread in the equator-to-pole surface temperature gradient.

5. Planetary Albedo and *ASR** in altered climate states

---

due to the hemispheric asymmetry in oceanic heat transport (there is 0.8 PW more ocean heat transport in the NH as compared to the SH). Whether the near balancing of the hemispheric asymmetry in *OLR** and ocean heat transport is casual, coincidental, or the consequence of an unrecognized constraint is an interesting question that is beyond the scope of the present work.

The previous sections have demonstrated that planetary albedo and *ASR** are largely insensitive to surface albedo. In this section, we explore the relationship between surface albedo, planetary albedo and ASR* in radically different climates that feature severely altered spatial patterns of surface albedo. We consider three additional model simulations of altered climate states: a T42 NCAR-CAM3 simulation of the Last Glacial Maximum (LGM) climate system (documented in Li and Battisti 2008), an equilibrated T42 NCAR-CAM3 simulation with four times the PI CO_2 concentration[11] (QUAD CO_2), and a GFDL-AM2.0 aquaplanet simulation coupled to a slab ocean that disallows the formation of sea ice (this run is identical to Kang et al. 2008, except with a 50m slab ocean). The meridional distribution of surface albedo varies widely in these runs (Figure 7a). The aquaplanet simulation has almost no meridional gradient in surface albedo[12]. The QUAD CO_2 simulation has a reduced high latitude surface albedo, relative to the PI run, due to a poleward shift in the ice edge. The LGM run has greatly enhanced surface albedo in the NH mid-latitudes mainly due to the presence of large continental ice sheets.

While the changes in sea ice extent and in the distribution of land ice surface in the altered climate states greatly affects the surface albedo, the changes in planetary albedo are much smaller than the changes in surface albedo. For example, in the mid-latitude NH, the surface albedo has increased from ~15% in the PI simulation to ~40% in the LGM experiment, but the surface contribution to the planetary albedo only increases by ~6%, from ~4% in the PI simulation to 10% in the LGM simulation (Figure 7b-c).

[11] The LGM and QUAD CO_2 runs are compared to a T42 CAM3 PI industrial run (the asterisk in Figures 5-6 and 9-11) as opposed to the T63 coupled CCSM3 PI run that is included in the CMIP3 ensemble.

[12] The small gradient in surface albedo is due to the angle of incidence dependence of ocean albedo.

Similarly, the mid-latitude and high-latitude total planetary albedo and surface contribution to planetary albedo in the QUA simulation changes (relative to the PI simulations) by approximately one third of the surface albedo change in the same regions. These simulations support the methodology we have employed and our interpretation of the results presented here; the changes in planetary albedo between the LGM, PI, and aquaplanet simulations agree with the changes in the surface contribution to planetary albedo assessed by our methodology. The complicating factor is that the cloud distributions do change (as we expect) in the altered climate states and these changes make a significant contribution to the planetary albedo. For example, the hemispheric average planetary albedo in the aquaplanet simulation (squares in Figure 5) is reduced relative to its AM2 PI counterpart simulation (Xs in Figure 5) due to nearly equal reductions in atmospheric and surface component contributions (Table 4). This result suggests that the atmospheric planetary albedo feedback due to moving from the Earth to an aquaplanet is comparable in magnitude to the radiative impact of the altered surface albedo itself.

Although we have concluded that surface processes play a secondary role in setting *ASR*,* in the present climate and do not contribute to the inter-model CMIP spread in *ASR**, the changes in surface albedo in the altered climate states make a significant contribution to the net change in *ASR**. For example, in the LGM simulation, *ASR** increases by 0.9 (0.4) PW in the NH (SH) relative to the PI NCAR-CAM3 run (Table 4). The *ASR** increase in the LGM is primarily due to a (0.5) PW increase in the surface contribution, a negligible change in the atmospheric contribution, and a 0.1 (0.1) PW decrease in the incident contribution associated primarily with the change global average

planetary albedo[13]. Similarly, *ASR** decreases by 4 (0.5) PW in the QUAD CO_2 runs relative to the CAM3 PI simulation. In contrast to the LGM *ASR** changes, both atmospheric and surface processes are responsible for the QUAD CO_2 changes in *ASR** with the atmosphere contributing a decrease of 0.2 (0.4) PW and the surface contributing a decrease of 0.2 (0.1) PW. These results suggest that, while the equatorward extent of the LGM ice edge significantly affects the equator-to-pole gradient in ASR, melting ice in the present climate system has very little potential to change the equator-to-pole gradient in ASR. For example, even if the CAM3 simulation had no gradient in surface albedo, *ASR** would only change by 0.3 PW in each hemisphere. In an ice free climate state, the changes in the cloudiness and atmospheric absorption will most likely overwhelm the more predictable changes in surface albedo. This result is in qualitative agreement with Kato et al.'s (2006) conclusion that the recent decline in Arctic sea ice has a negligible signature on the Arctic radiative budget at the TOA due to atmospheric attenuation.

The aquaplanet simulation demonstrates that eliminating the surface albedo gradient altogether has a fairly small effect on the equator-to-pole gradient of ASR: relative to the GFDL-CM2 PI simulation the GFDL-AM2 aquaplanet simulation actually exhibits a net increase in *ASR** of 0.5 PW in the SH and a decrease of 0.2 PW in the NH (Table 4). As expected, eliminating the surface albedo gradient in the aquaplanet simulation eliminates the surface albedo contribution to *ASR*,* resulting in a decrease in

[13] The change in obliquity enhances the incident contribution to ASR* in the LGM, but this change is overwhelmed by the effect of the enhanced global average planetary albedo that acts to decrease the incident contribution to ASR* (see Equation 3).

*ASR** of 0.4 (0.3) PW in the NH (SH). However, changes in cloud reflection overwhelm this change in the SH, contributing an additional 0.5 PW to ASR* for the aquaplanet simulation. In the NH, clouds diminish ASR* by 0.1 PW relative to the PI run[14]. This result again suggests that eliminating sea ice in the current climate would have little effect on the existing equator-to-pole gradient in ASR but the concurrent changes in cloud properties would make a larger (and more uncertain) contribution to the equator-to-pole gradient in forcing so that the sign of the change in *ASR** is uncertain, even in an ice free world.

6. Summary and Discussion

In both the observed and modeled climate system, more than 85% of the global average planetary albedo is due to atmospheric reflection as opposed to surface reflection of solar radiation. The CMIP3 ensemble inter-model spread of global average planetary albedo is also primarily due to differences in atmospheric reflection. Surface albedo has a small effect on planetary albedo because clouds are highly reflective and the atmosphere is somewhat opaque to solar radiation; hence, the impact of the surface albedo is strongly attenuated by the atmosphere.

Approximately 65% (60%) of the observed equator-to-pole gradient in ASR in the NH (SH) is a consequence of the meridional distribution of incident solar radiation at the TOA while the remaining 35% (40%) results from the meridional distribution of planetary albedo. We have demonstrated that the vast majority (86% and 89% in the NH

[14] The incident contribution to *ASR** in the aquaplanet simulation is enhanced by 0.3 PW in both hemispheres due to the reduced global average planetary albedo (see Equation 3).

and SH) of the meridional gradient of planetary albedo is a consequence of atmospheric as opposed to surface processes. These results suggest that surface albedo plays a significantly smaller role in forcing the climate system on the equator-to-pole scale than atmospheric reflection (e.g. cloud distribution) and atmospheric absorption. These results are contingent upon the reliability of the CERES surface radiative fluxes which are known to have trouble retrieving cloud reflectance over ice surfaces (Rutan et al. 2001). There is evidence that our methodology may overestimate the solar reflectance of clouds over Antarctica; the small meridional gradient in atmospheric reflection between the Southern Ocean and the South Pole seen in our Figure 4a is qualitatively at odds with the large meridional gradient in cloud optical properties (with larger optical thickness over the Southern Ocean) found over the same region by Fitzpatrick and Warren (2007). Despite these regional discrepancies, the general agreement of the models and observations on the partitioning of ASR^* between atmospheric and surface processes suggests that the CERES surface solar fluxes are reliable for the purpose of our study.

The total equator-to-pole gradient in absorbed solar radiation, ASR^*, and its partitioning into atmospheric and surface albedo components found in the observations is well replicated in the multi-model mean of the CMIP3 PI model simulations. However, there are substantial differences (of order 20%) in the equator-to-pole gradient of ASR in the models. We have demonstrated that the vast majority of this spread results from inter-model differences in the meridional profiles of the reflection of solar radiation within the atmosphere which we believe results from differences in the cloud distributions simulated by the models. We have also found that the inter-model spread in maximum MHT is largely due to the inter-model spread in the meridional gradient of ASR, such that the

total heat transport in the climate models is primarily determined by the optical properties of the atmosphere.

These results have implications for the role of the ice albedo feedback in forcing climate on the equator-to-pole scale in altered climate states (i.e. global warming and glacial states). It is commonly stated that the ice albedo feedback is the leading cause of the polar amplification of anthropogenic climate change (IPCC 2007, Hansen et al. 1997, and Hall 2004). Our work suggests that surface albedo plays a secondary role to atmospheric processes in determining both the climatology and inter-model variability of the equator-to-pole gradient in ASR and equator-to-pole gradient of net shortwave radiation at the surface (not shown). Although this study does not directly address the global warming problem, we note that, even in the extreme situation of the surface albedo gradient going to zero (i.e. all ice melts), the impact on ASR^* would be small compared to the inter-model spread in ASR^* due to atmospheric reflectance. This suggests that cloud distribution changes in altered climate states are likely to play a more important role in setting the meridional gradient of ASR than even zeroth order changes in surface albedo (Eastman and Warren 2010).

Our results indicate that in the present climate the peak MHT is mainly determined by the shortwave optical properties of the atmosphere (i.e. cloud distribution) and suggests that MHT is largely insensitive to subtleties in the model dynamics that contribute to the heat transport. The MHT is primarily a result of the mispheric scale distribution of absorbed radiation while the specifics of heat transport dynamics are less important (Stone 1978). We can understand this result in the context of simplified energy balance models. In the annual mean, the extratropical deficit in ASR, ASR^*, is balanced

by the sum of OLR anomalies relative to the global mean (*OLR**) and meridional heat transport into the extratropics (MHT). If the heat transport is diffusive along the surface temperature gradient and the OLR anomaly is proportional to the surface temperature anomaly from the global mean (as in Held 1982 amongst others) then both the extratropical OLR anomaly and MHT are proportional to the same equator-to-pole temperature gradient. The ratio between MHT and *OLR** is then dictated by the relative efficiencies of large scale heat diffusion and radiation to space which is commonly called δ in the literature (see Rose and Marshall 2009 for a review). If two climate models had different δ values yet the same *ASR**, the peak MHT would differ between the models. For example, a more diffusive model (e.g. a model with more vigorous baroclinic eddies) would have more MHT and less *OLR** and vice versa. In contrast, if this ratio were nearly equal amongst climate models, then the MHT would be proportional to *ASR**. We speculate that the CMIP3 suite of climate models all have a similar δ value such that MHT is dictated by *ASR** which in turn, we have demonstrated is controlled by the meridional distribution of clouds simulated.

It is interesting to note that, in the altered climate state simulations, changes in *ASR** do *not* track one-to-one to changes in MHT. For example, the 0.9 PW increase in *ASR** in the LGM NH only leads to a 0.3 PW increase in MHT, with the remaining 0.6 PW balanced by *OLR**. We speculate that this result is a consequence of the climate state dependence of δ; δ is reduced in a colder and drier planet because the atmosphere is more transparent to longwave radiation and thus more efficient at radiating longwave energy to space and the drier atmosphere is less efficient at transporting energy meridionally

(Frierson et al. 2007). We hope to examine inter-model, seasonal, and inter-climate state variability of δ more formally and rigorously in future work.

Acknowlegements

Dargan Frierson ran the seasonal aquaplanet simulation utilized in this work and provided feedback on the discussion in this text. Camille Li ran and provided the model output for the LGM and QUAD CO_2 runs. Stephen Warren's advice on the observational data sets used and comments were greatly appreciated. Tra Dinh and Tom Ackerman provided a radiative transfer model that aided in verifying our methodology and were also instrumental aids in understanding the radiative components of this work. This work was inspired by conversations with Gerard Roe, Kyle Armour, Ed Wrigglesworth Blanchard IV, Brian Rose, John Marshall, Valerio Lucarini, Rowan Sutton and Jonathan Gregory.

References

Barkstrom, B., E. Harrison, G. Smith, R. Green, J. Kibler, and R. Cess, The ERBE Science Team, 1989: Earth Radiation Budget (ERBE) archival and April 1985 results. *Bull. Amer. Meteor. Soc*., 70, 1254-1262.

Bony, S., and coauthors, 2006: How well do we understand climate change feedback processes? *J. Climate*, 19, 3445-3482.

Budyko, M.I., 1969: The effect of solar radiation variations on the climate of the Earth. *Tellus*, 21, 611-619.

Chou M.D. and K.T. Lee, 1996: Parameterizations for the absorption of solar radiation by water vapor and ozone. *J. Atmos. Sci.*, 53, 1203-1208.

CLIMAP project members, 1981: Seasonal reconstruction of the Earth's surface at the last glacial maximum. Geological Society of America Map and Chart Series, No. 36, 18pp.

Curry, J.A., W.B. Rossow, D. Randall, and J.L. Scramm, 1996: Overview of Arctic cloud radiation characteristics. *J. Climate*, 9: 1731-1762.

Dong, B.W., and P.J. Valdes, 1995: Sensitivity studies of Northern Hemisphere glaciation using an atmospheric general circulation model. *J. Climate*, 8, 2471–2496.

Eastman R. and S.G. Warren, 2010: Interannual variations of Arctic cloud types in relation to sea ice. *J. Climate*, In press.

Enderton, D. and J. Marshall, 2009: Controls on the total dynamical heat transport of the atmosphere and oceans. *J. Atmos. Sci.,* 66, 1593-1611

Fitzpatrick, M.F. and S.G. Warren, 2007: The relative importance of clouds and sea ice for the solar energy budget of the Southern Ocean. *J. Climate*, 20, 941-954.

Frierson, D. M. W., Held, I. M. and P. Zurita-Gotor, 2007. A Gray-Radiation Aquaplanet Moist GCM. Part II: Energy Transports in Altered Climates. *J. Atmos. Sci.,* 64, 1680-1693.

Gorodetskaya, I. V., M. A. Cane, L-B. Tremblay, and A. Kaplan, 2006: The effects of sea ice and land snow concentrations on planetary albedo from the Earth Radiation Budget Experiment. *Atmos.–Ocean*, 44:195–205.

Graves, C.E., W.-H. Lee, and G.R. North, 1993: New parameterizations and sensitivities for simple climate models. *J. Geophys. Res.*, 98, 5025-5036.

Hahn, C.J., and S.G. Warren, 2003: Cloud climatology for land stations worldwide, 1971-1996. Numerical Data Package NDP-026D, Carbon Dioxide Information Analysis Center (CDIAC), Department of Energy, Oak Ridge, Tennessee (Documentation, 35 pages).

Hall A., 2004: The role of surface albedo feedback in climate. *J. Climate*, 17:1550–1568.

Hansen J., M. Sato, R. Ruedy, 1997: Radiative forcing and climate response. *J. Geophys. Res*., 102(D6), 6831–6864.

Hartmann, D.L., 1994: Global Physical Climatology. Academic Press, 411 pages.

Held I.M. and M.J. Suarez, 1974: Simple albedo feedback models of the icecaps. *Tellus*, 26, 613-629.

IPCC, 2007: Climate Change 2007: The Physical Science Basis. Contribution of Working Group I to the Fourth Assessment Report of the Intergovernmental Panel on Climate Change [Solomon, S., D. Qin, M. Manning, Z. Chen, M. Marquis, K.B. Averyt, M.Tignor and H.L. Miller (eds.)]. Cambridge University Press, Cambridge, United Kingdom and New York, NY, USA.

Kang S.M., I.M. Held, D.M.W. Frierson, and M. Zhao, 2008: The Response of the ITCZ to extratropical thermal forcing: idealized slab-ocean experiments with a GCM. *J. Climate*, 21, 3521-3532.

Kato, S., N.G. Loeb, P. Minnis, J.A. Francis, T.P. Charlock. D.A. Rutan, E.E. Clothiaux, and S. Sun-Mack, 2006: Seasonal and interannual variations of top-of-atmosphere irradiance and cloud cover over polar regions derived from CERES data set. *Geophys. Res. Lett.*, 33, L19804 doi:10.1029/2006GL026685.

Kato, S., T.P Ackerman, J.H. Mather, and E Clothiaux, 1999**:** The *k*-distribution method and correlated-*k* approximation for a shortwave radiative transfer model. *Journal of Quanitative Spectroscopy and Radiative Transfer*, 62, 109-121.

Li C. and D.S. Battisti, 2008: Reduced Atlantic storminess during Last Glacial Maximum: evidence from a coupled climate model, *J. Climate*, 21, 3561-3579.

Lucarini, V. and F. Ragone, 2010: Energetics of IPCC4AR4 climate models: energy balance and meridional enthalpy transports. Submitted to *Rev. Geophys*.

Meehl, G. A., C. Covey, T. Delworth, M. Latif, B. McAvaney, J. F. B. Mitchell, R. J. Stouffer, and K. E. Taylor, 2007: The WCRP CMIP3 multi-model dataset: A new era in climate change research, *Bull. Amer. Meteor. Soc.*, 88, 1383-1394.

Minnett, P. J., 1999: The influence of solar zenith angle and cloud type on cloud radiative forcing at the surface in the Arctic. *J. Climate*, 12, 147–158.

North, J.R, 1975: Theory of energy-balance climate models. *J. Atmos. Sci.*, 32, 1189-1204.

Phillips, P.J. and I.M. Held, 1994: The response to orbital perturbations in an atmospheric model coupled to a slab ocean. *J. Climate*, 7, 767-782.

Pierrehumbert, R.T., 2005: Climate dynamics of a hard snowball Earth. *J. Geophys. Res.*, 110(D1) D01111 doi:10.1029/2004JD005162.

Qu, X. and A. Hall, 2005: Surface contribution to planetary albedo variability in the cryosphere regions. *J. Climate*, 18, 5239-5252.

Robock, A., 1980: The seasonal cycle of snow cover, sea ice and surface albedo. *Mon.Wea. Rev.*, 108, 267-285.

Rose, B.E.J and J. Marshall, 2009: Ocean heat transport, sea ice, and multiple climate states: insights from energy balance models. *J. Atm. Sci.*,66, 2828--2843.

Rutan, D.A., F.G. Rose, N.M. Smith, T.P. Charlock, 2001: Validation data set for CERES surface and atmospheric radiation budget (SARB), WCRP/GEWEX Newsletter, Vol 11, No. 1, 11-12.

Stone, P.H. 1978: Constraints on dynamical transports of energy on a spherical planet. *Dyn. Atmos. Oceans*, 2, 123-139.

Taylor, K.E. M. Crucifix, P. Braconnot, C.D. Hewitt, C. Doutriaux, A.J. Broccoli, J.F.B. Mitchell and, M.J. Webb, 2007: Estimating shortwave radiative forcing and response in climate models. *J. Climate*, 20, 2530-2543.

Trenberth, K. E., and J. M. Caron, 2001: Estimates of meridional atmosphere and ocean heat transports. *J. Climate*, 14, 3433–3443.

Warren, S.G., and S.H. Schneider, 1979. Seasonal simulation as a test for uncertainties in the parameterizations of a Budyko-Sellers zonal climate model. *J. Atmos. Sci.*, 36, 1377-1391.

Wielicki, B, R.D. Cess, M.D. King, D.A. Randall, and E.F. Harrison, 1995: Mission to planet Earth – role of clouds and radiation in climate. *Bull. Am. Meteor. Soc.*, 76, 2125-2153.

Zhou T. , B. Wu, X. Wen, L. Li, and B. Wang, 2008: A fast version of LASG/IAP climate system model and its 1000-year control integration. *Adv. Atms. Sci.*, 25, 655-672.

Figure Captions

Figure 1. (a) Graphical demonstration of *ASR**. Observed zonal mean ASR (solid black line) co-plotted with the global mean ASR (dashed black). The black asterisks denote the latitude where ASR = 0 in each hemisphere and the blue area is *ASR**. (b) Partitioning of zonal mean ASR into the three terms in equation 2. (c) As in (b) except combining the 2nd and 3rd terms in Equation 2 such that the total ASR is partitioned into a component that exists in the absence of a spatial structure in planetary albedo and a term associated with planetary albedo gradients as discussed in the text. (d) The spatial integrals of the curves in (c) over the extratropics in each hemisphere which define the component contributions to *ASR**.

Figure 2. Schematic representing the first two reflections in the single layer solar radiation model. Moving from left to right, the arrows represent the radiative fluxes associated with the incident solar, first reflection, and second reflection. A, R, and α are the atmospheric absorption fraction during a single pass through the atmosphere, the fraction of cloud reflection, and the surface albedo respectively. The solid (dashed) arrows at the TOA represent the radiative fluxes we associated with cloud (surface) reflection.

Figure 3. (a and c) The surface albedo and planetary albedo, expressed as a percent. (b and d) The surface ($\frac{\alpha\ (1-R-A)^2}{1-\alpha R}$) and atmospheric ($R$) contribution to planetary albedo expressed as a percent of the incident solar radiation as described in the text.

Figure 4. (a) Zonal mean planetary albedo partitioned between atmospheric and surface components. (b) Zonal mean surface albedo and "effective" surface albedo. (c) Atmospheric attenuation of surface albedo.

Figure 5. (a) Hemispheric average planetary albedo versus atmospheric contribution to hemispheric average planetary albedo in the NH and SH (blue and red plus signs) of the CMIP3 PI model ensemble, observations (filled squares), and additional model simulations. The dashed lines are linear best fits to the PI simulations and the solid line is the 1:1 line with zero intercept. (b) as in (a) except plotted against surface albedo contribution to hemispheric average planetary albedo.

Figure 6. Hemispheric average planetary albedo versus hemispheric average surface albedo in the NH and SH (blue and red symbols) for the CMIP3 ensemble, observations, and altered climate states. The axes have a 1:1 ratio. The dashed lines are the linear best fits to the PI simulations in each hemisphere.

Figure 7. Zonal annual mean (a) surface albedo, (b) planetary albedo, (c) surface contribution to planetary albedo, and (d) atmospheric contribution to planetary albedo in the CMIP3 multi-model ensemble of PI simulations (dashed black lines). Also shown are the observations (solid, light blue) and model simulations of altered climate states (colored lines).

Figure 8. The inter-model standard deviation of zonal average planetary albedo (solid line), atmospheric contribution to planetary albedo (dashed line) and, surface contribution to planetary albedo (dashed-dot line) for the CMIP3 PI simulations.

Figure 9. (a) *ASR** versus atmospheric contribution to *ASR** in each the NH and SH (blue and red plus signs) of the CMIP3 PI model ensemble, observations (filled squares), and additional model simulations. The theoretical prediction of "Model A", as discussed in the text, is given by the black line. (b) as in (a) except plotted against surface albedo contribution to *ASR**.

Figure 10. The equator-to-pole difference in ASR, *ASR**, versus the equator-to-pole difference surface albedo, *SURF**. The black line represents the prediction of "Model B" as discussed in the text.

Figure 11. (a) MHT versus atmospheric contribution to *ASR** in each hemisphere of the CMIP3 PI ensemble, observations, and additional model simulations. The blue (red) lines are the linear best fits to the PI model simulations in the NH (SH). (b) *TS** versus *ASR**.

Tables and Table Captions

Table 1. Global average planetary albedo, its decomposition into atmospheric and surface components (as described in the text), and global average surface albedo for the observations and the CMIP3 multi-model average and spread (2 standard deviations). All entries are in percent units.

(%)	Total	Atmospheric	Surface	Surface Albedo
Observations	31.3	27.7	3.6	11.7
Model Average	30.4	26.4	4.0	13.2
Model Spread (2σ)	1.6	2.3	1.3	3.1

Table 2. *ASR**, its partitioning into incident and planetary albedo components (2nd and 3rd columns) by application of Equation 3 and the subsequent partitioning of the planetary albedo component into atmospheric and surface contributions (4th and 5th columns) by application of Equation 7. *OLR** and the peak MHT are also shown. The observations and CMIP3 multi-model average and spread (2 standard deviations) are shown for each hemisphere. All entries are in PWs.

(PW)	Total *ASR**	Incident	Albedo	Atmospheric	Surface	*OLR**	MHT
NORTHERN HEMISPHERE							
Observations	8.1	5.2	2.9	2.5	0.4	2.4	5.7
Model Average	8.1	5.2	2.9	2.4	0.5	2.6	5.5
Model Spread (2σ)	0.9	0.1	0.9	1.2	0.5	0.6	0.8
SOUTHERN HEMISPHERE							
Observations	8.7	5.2	3.5	3.1	0.4	3.2	5.5
Model Average	8.4	5.2	3.2	2.9	0.3	3.2	5.2
Model Spread (2σ)	1.2	0.1	1.2	1.4	0.4	0.5	1.1

Table 3. Models used in this study and their resolution.

Abbreviation	Full Name	Horizontal Resolution	Vertical Resolution
BCCR-BCM2.0	Bjerknes Centre for Climate Research, University of Bergen Norway	T63	L31
CCCMA-CGCM3.1	Canadian Centre for Climate Modeling & Analysis, Canada	T47	L31
CNRM-CM3	Meteo-France/Centre National de Recherches ´te´orologique, France	T63	L45
CSIRO-MK3.0	Australian Commonwealth Scientific and Research Organization (CSIRO), Australia	T63	L18
GFDL-CM2.0	NOAA/Geophysical Fluid Dynamics Laboratory, USA	X 2.5	L24
GISS-ER	NASA/Goddard Institute for Space Studies, USA	4 X 5	L20
IAP-FGOALS	National Key Laboratory of Numerical Modeling for Atmospheric Sciences and Geophysical Fluid Dynamics (LASG), China	T42	L26
MPI-ECHAM5	Max Planck Institute for Meteorology, Germany	T63	L31
INM-CM3.0	Institute for Numerical Mathematics, Russia	4 X 5	L21
IPSL-CM4.0	Institute Pierre Simon Laplace, France	2.5 X 3.75	L19
Micro3.2 (Hires)	National Institute for Environmental Studies, and Frontier Research Center for Global Change, Japan	T106	L56
MRI-CGCM2.3.2a	Meteorological Research Institute, Japan	T42	L30
NCAR-CCSM3.0	National Center for Atmospheric Research, USA	T85	L26
UKMO-HADCM3	Hadley Centre for Climate Prediction and Research/Met Office, UK	2.5 X 3.8	L19
MIUB-ECHOg	University of Bonn, Germany	T30	L19

Table 4. Change in hemispheric average planetary albedo and equator-to-pole contrast of ASR, *ASR**, and the partitioning of the changes into atmospheric and surface contributions in the altered climate state simulations. Each difference is taken relative to the PI simulation in the same model used to simulate the altered climate state (and at the same resolution). Also shown are *OLR** and the peak meridional heat transport (MHT) changes. The last two rows show the CMIP3 inter-model spread (2σ) of the same variables.

Model /Hemisphere		Hemispheric Average Planetary Albedo (%)			Equator-to-pole Contrast					
					ASR* (PW)				OLR* (PW)	MHT (PW)
		Total	Atmos	Surface	Total	Atmos	Surf	incident		
QUAD – PI	NH	-0.2	+0.4	-0.6	-0.4	-0.2	-0.2	0.0	-0.3	-0.1
	SH	-0.3	+0.1	-0.4	-0.5	-0.4	-0.1	0.0	-0.1	-0.3
LGM –PI	NH	+2.2	+0.6	+1.6	+0.9	0.0	+1.0	-0.1	+0.6	+0.3
	SH	+1.9	+1.1	+0.8	+0.4	0.0	+0.5	-0.1	+0.3	+0.1
AQUA – PI	NH	-4.2	-1.8	-2.4	-0.2	-0.1	-0.4	+0.3	+0.5	-0.7
	SH	-3	-1.5	-1.5	+0.5	+0.5	-0.3	+0.3	+0.2	+0.3
CMIP 2σ	NH	1.8	2.7	1.4	0.9	1.2	0.5	0.1	0.6	0.8
	SH	1.8	2.1	1.1	1.2	1.4	0.4	0.1	0.5	1.1

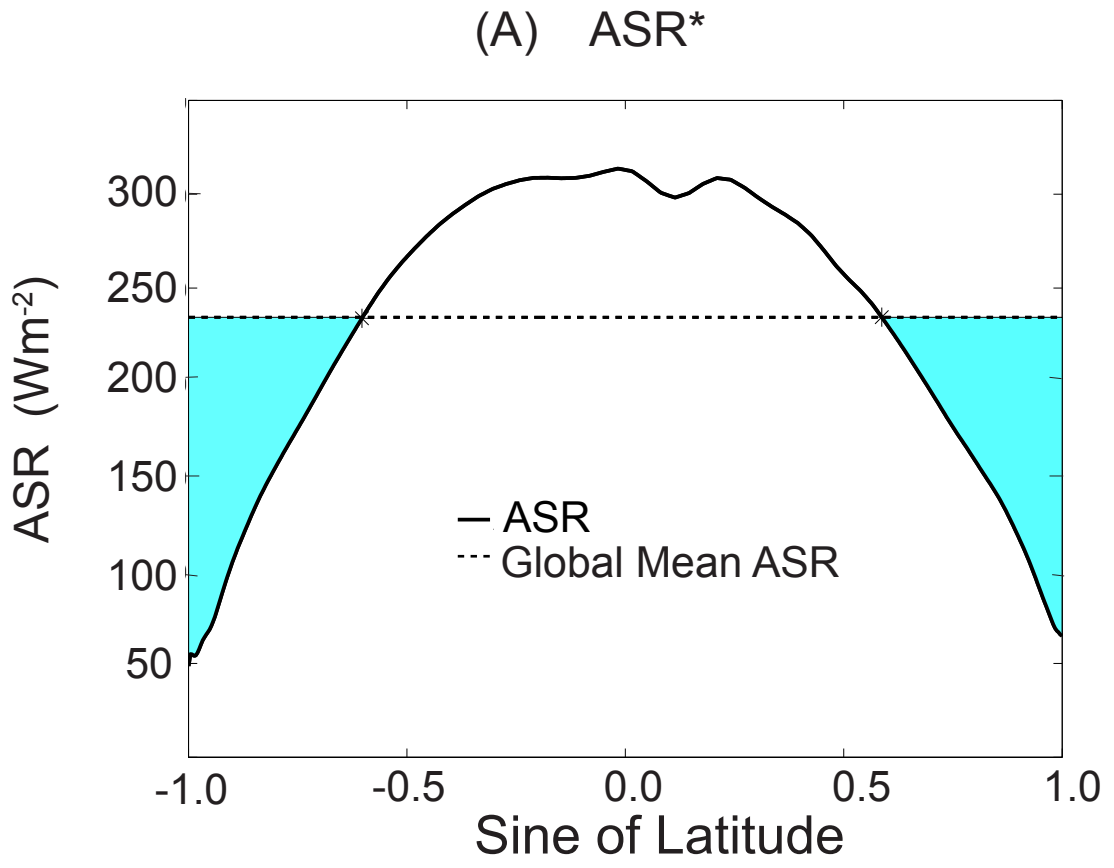

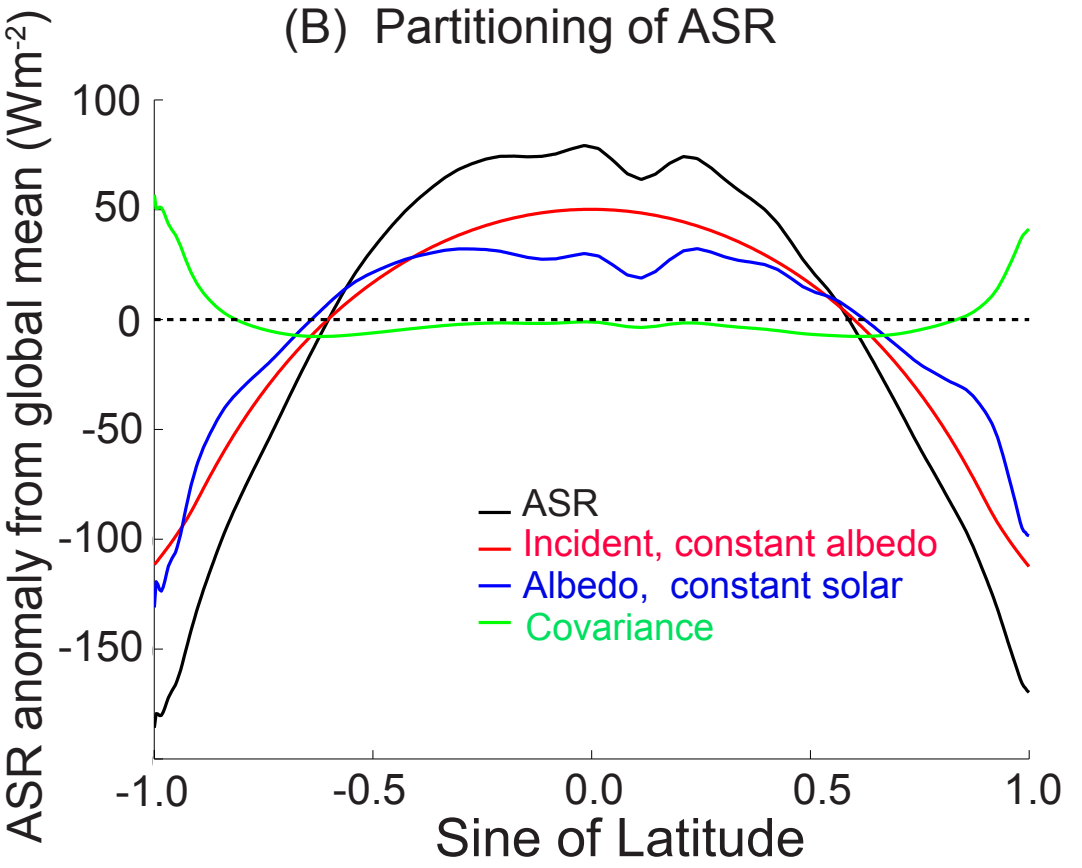

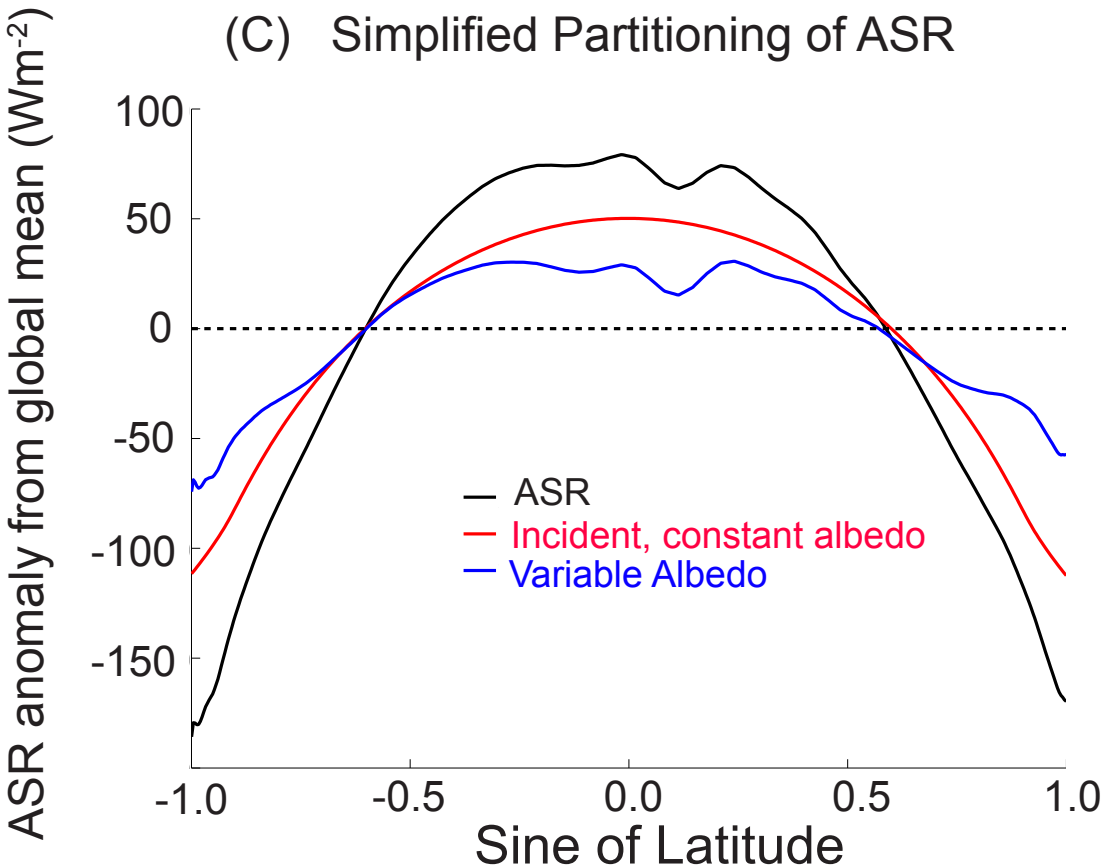

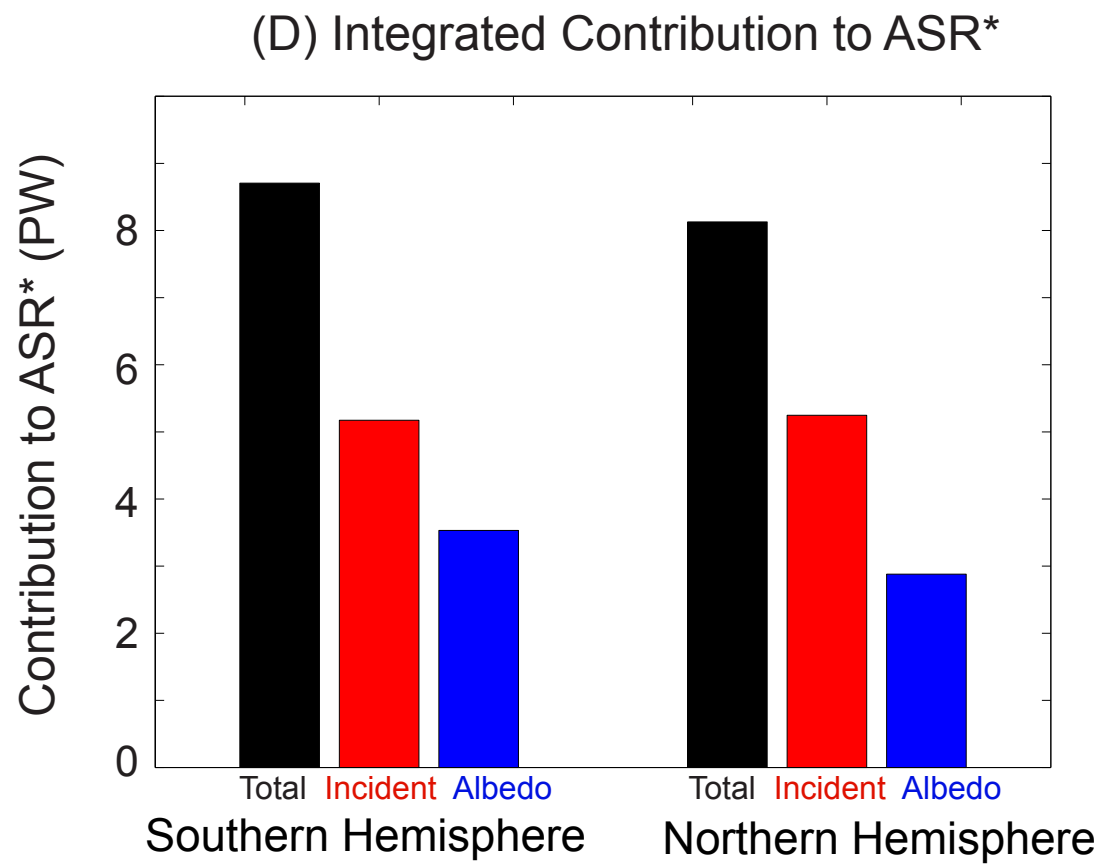

Figure 1. (a) Graphical demonstration of ASR*. Observed zonal mean ASR (solid black line) co-plotted with the global mean ASR (dashed black). The black asterisks denote the latitude where ASR' = 0 in each hemisphere and the blue area is ASR*. (b) Partitioning of zonal mean ASR into the three terms in equation 2. (c) As in (b) except combining the 2nd and 3rd terms in Equation 2 such that the total ASR' is partitioned into a component that exists in the absence of a spatial structure in planetary albedo and a term associated with planetary albedo gradients as discussed in the text. (d) The spatial integrals of the curves in (c) over the extratropics in each hemisphere which define the component contributions to ASR*.

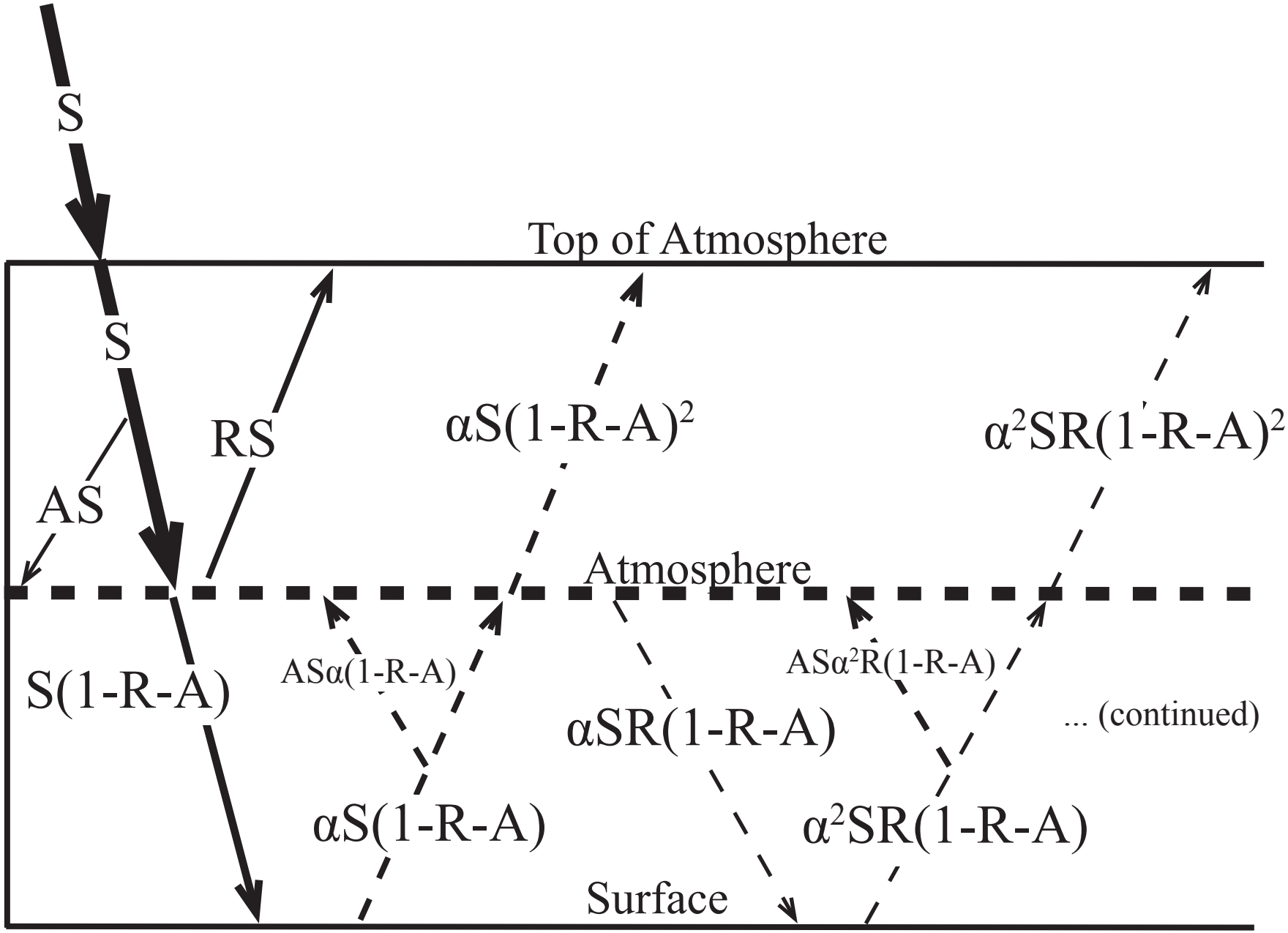

Figure 2. Schematic representing the first two reflections in the single layer solar radiation model. Moving from left to right, the arrows represent the radiative fluxes associated with the incident solar, first reflection, and second reflection. A, R, and α are the atmospheric absorption fraction during a single pass through the atmosphere, the fraction of cloud reflection, and the surface albedo respectively. The solid (dashed) arrows at the TOA represent the radiative fluxes we associated with cloud (surface) reflection.

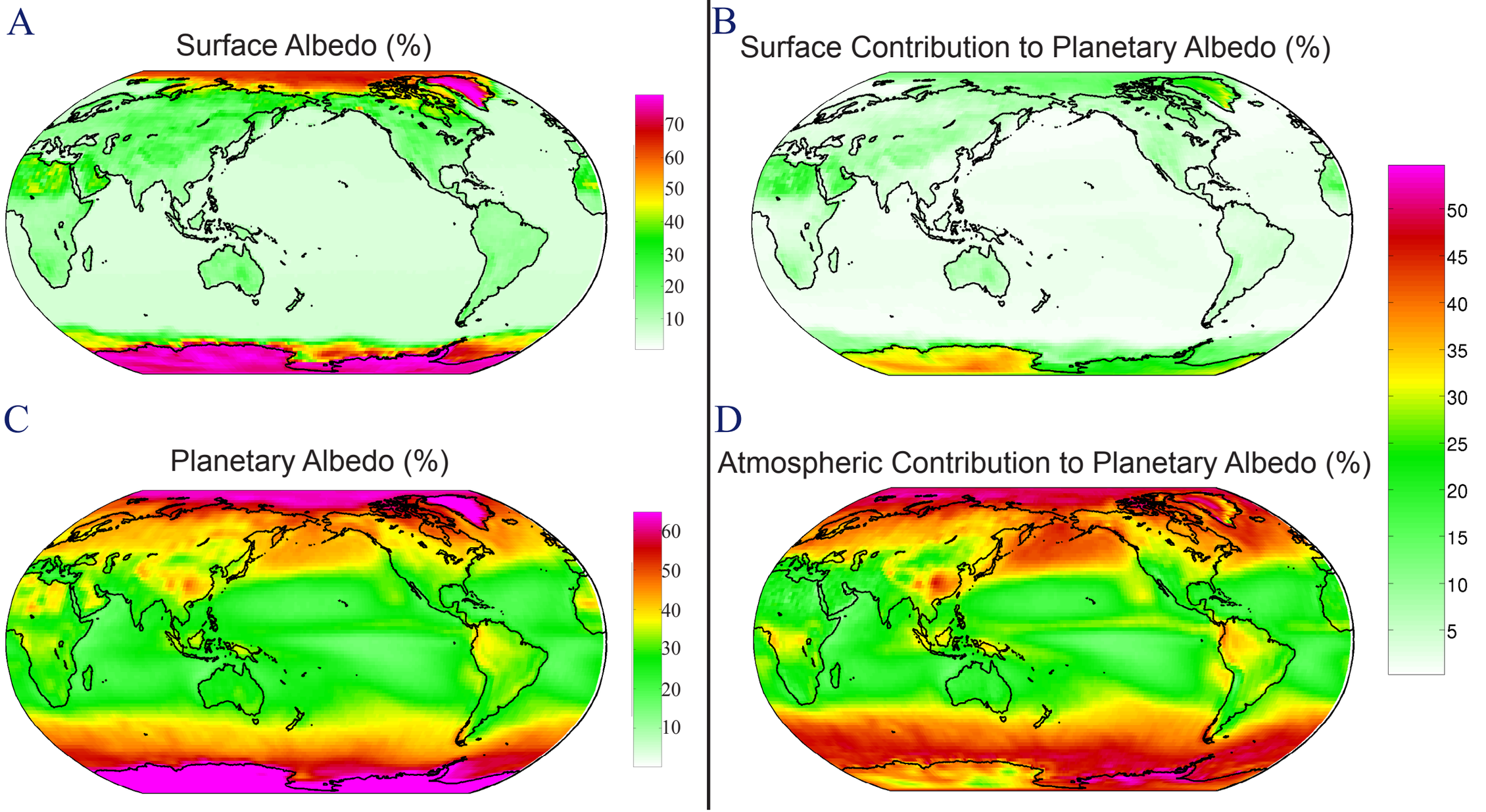

Figure 3. (a and c) The surface albedo and planetary albedo, expressed as a percent. (b and d) The surface ($\frac{\alpha\ (1-R-A)^2}{1-\alpha R}$) and atmospheric (R) contribution to planetary albedo expressed as a percent of the incident solar radiation as described in the text.

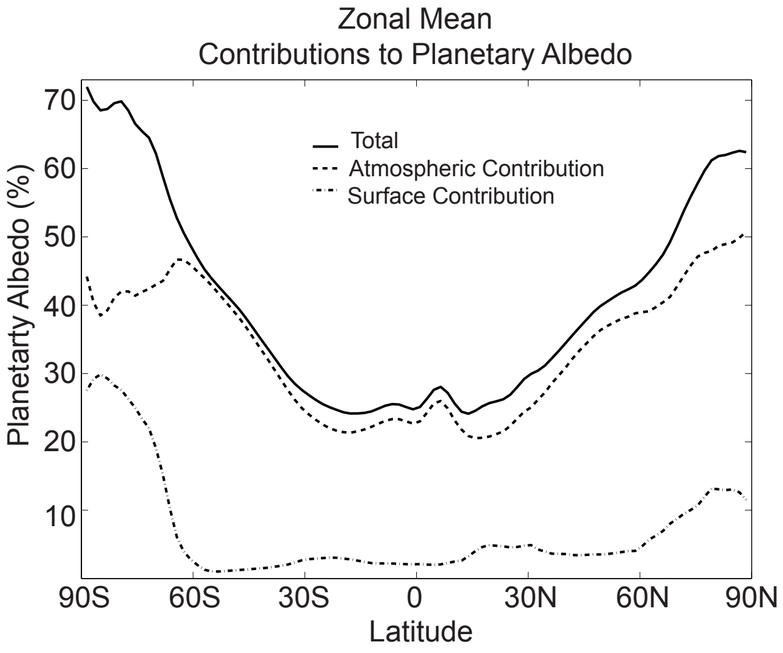

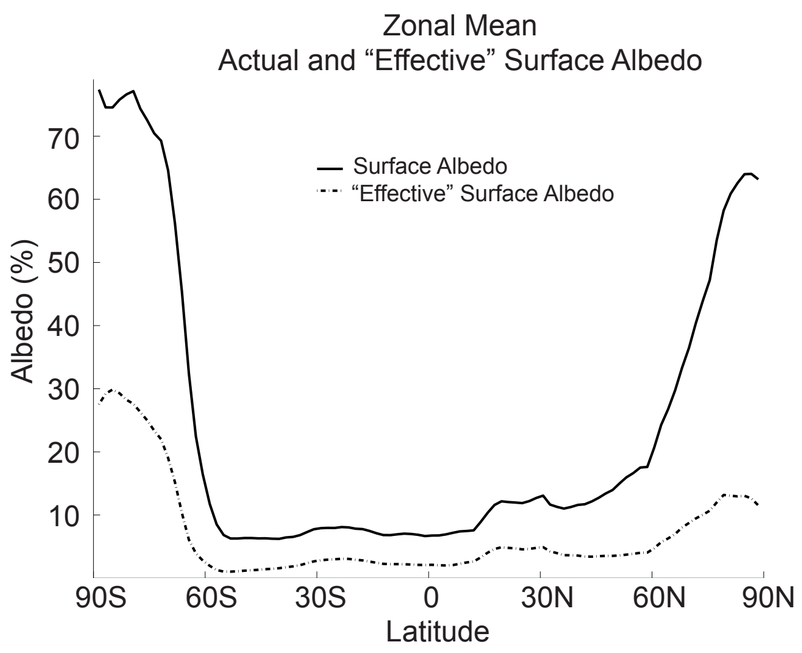

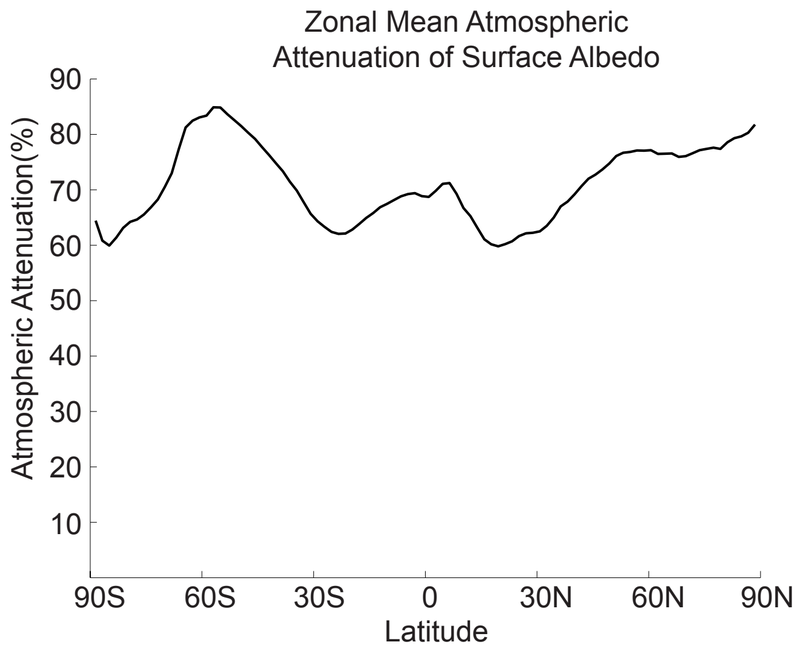

Figure 4. (a) Zonal mean planetary albedo partitioned between atmospheric and surface components. (b) Zonal mean surface albedo and “effective” surface albedo. (c) Atmospheric attenuation of surface albedo.

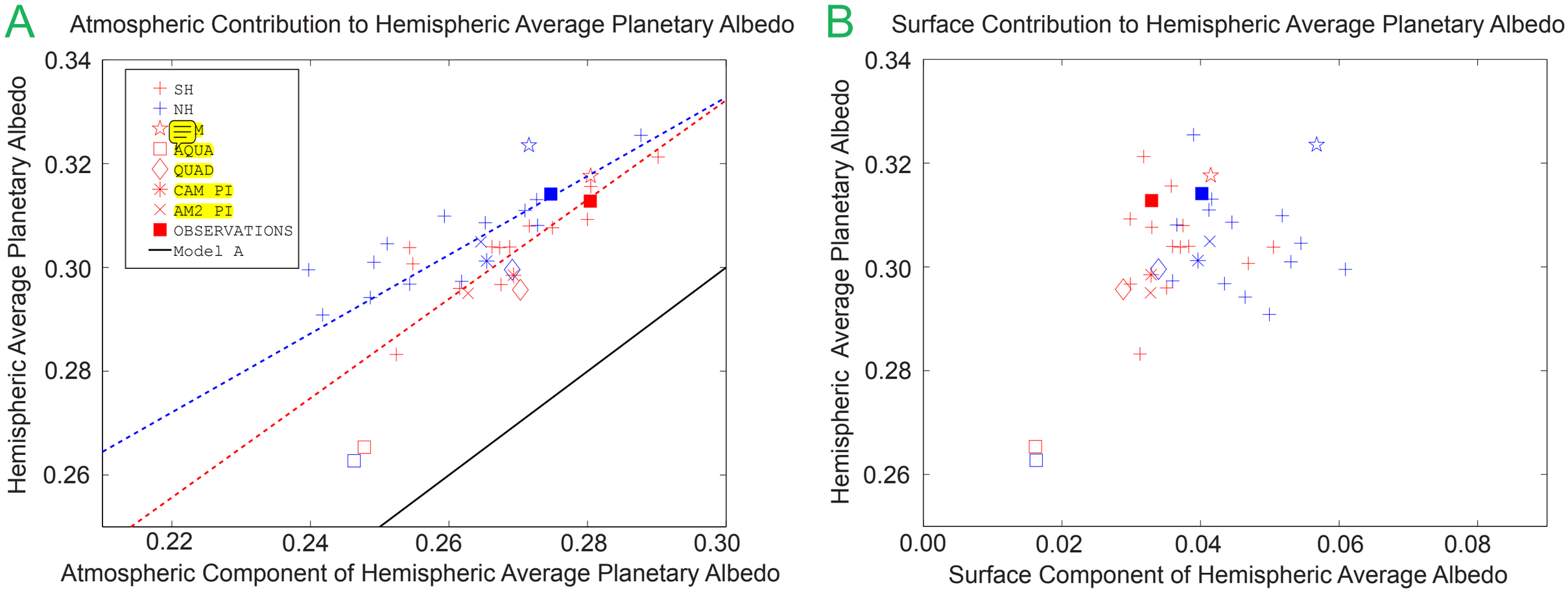

Figure 5. (a) Hemispheric average planetary albedo versus atmospheric contribution to hemispheric average planetary albedo in the NH and SH (blue and red plus signs) of the CMIP3 PI model ensemble, observations (filled squares), and additional model simulations. The dashed lines are linear best fits to the PI simulations and the solid line is the 1:1 line with zero intercept. (b) as in (a) except plotted against surface albedo contribution to hemispheric average planetary albedo.

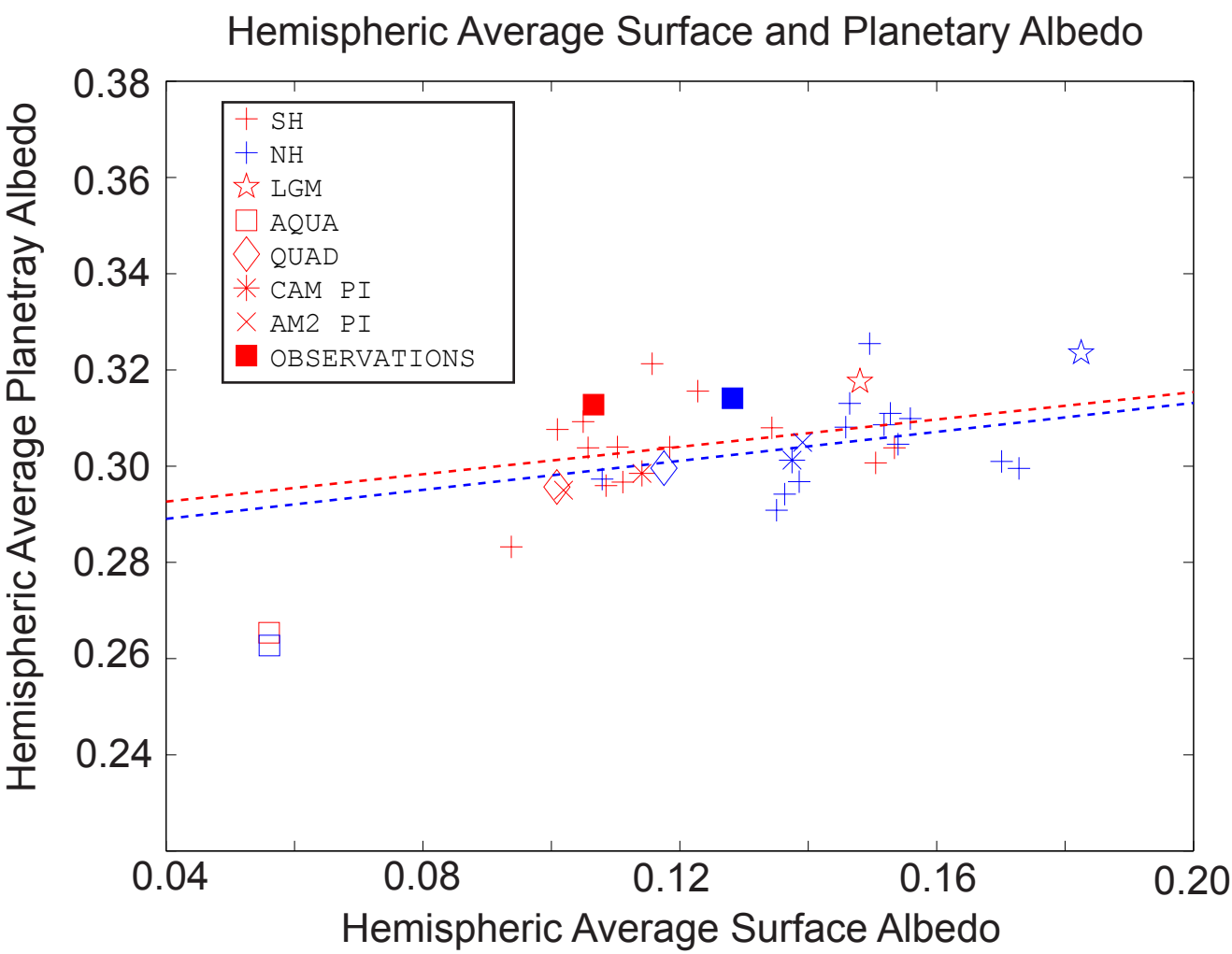

Figure 6. Hemispheric average planetary albedo versus hemispheric average surface albedo in the NH and SH (blue and red symbols) for the CMIP3 ensemble, observations, and altered climate states. The axes have a 1:1 ratio. The dashed lines are the linear best fits to the PI simulations in each hemisphere.

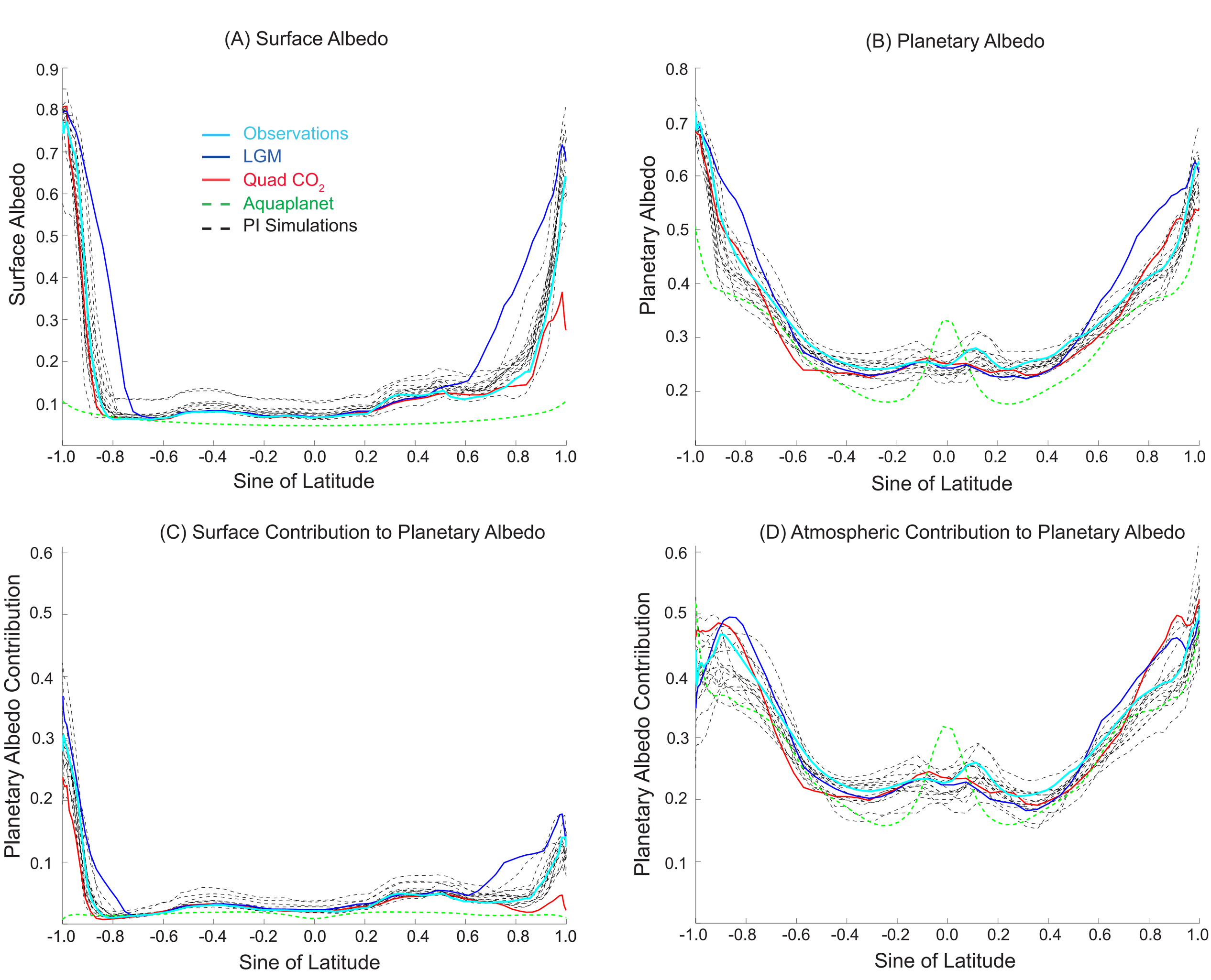

Figure 7. Zonal annual mean (a) surface albedo, (b) planetary albedo, (c) surface contribution to planetary albedo, and (d) atmospheric contribution to planetary albedo in the CMIP3 multi-model ensemble of PI simulations (dashed black lines). Also shown are the observations (solid, light blue) and model simulations of altered climate states (colored lines).

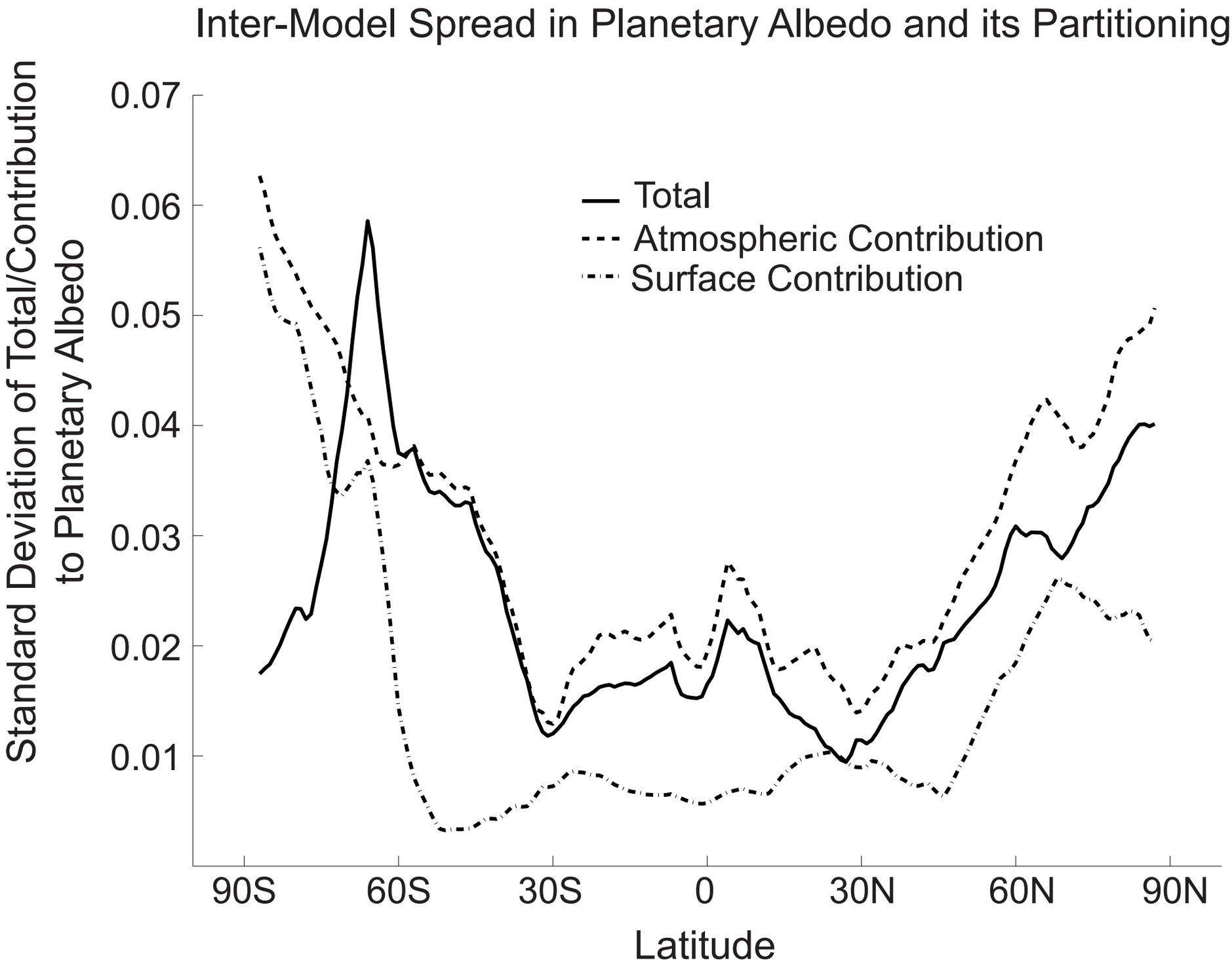

Figure 8. The inter-model standard deviation of zonal mean planetary albedo (solid line), atmospheric contribution to planetary albedo (dashed line) and, surface contribution to planetary albedo (dashed-dot line) for the CMIP3 PI simulations.

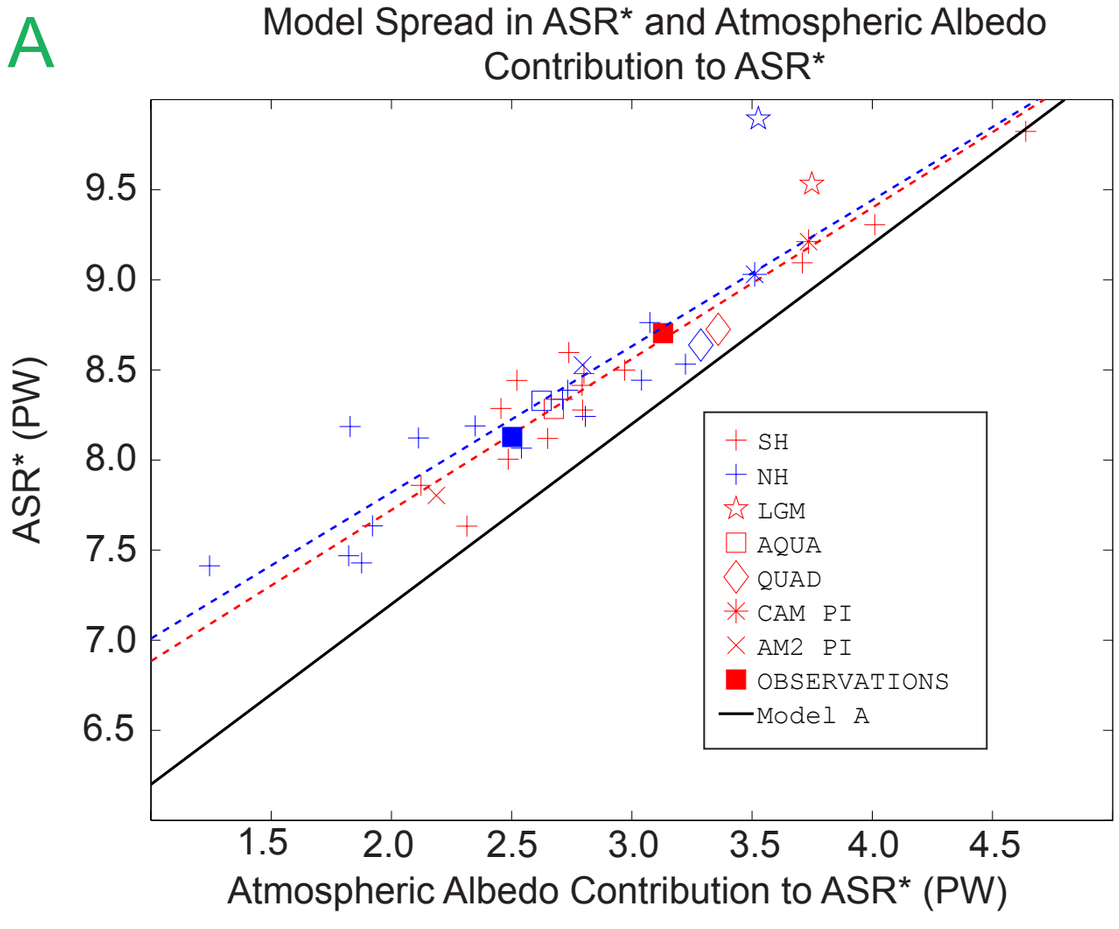

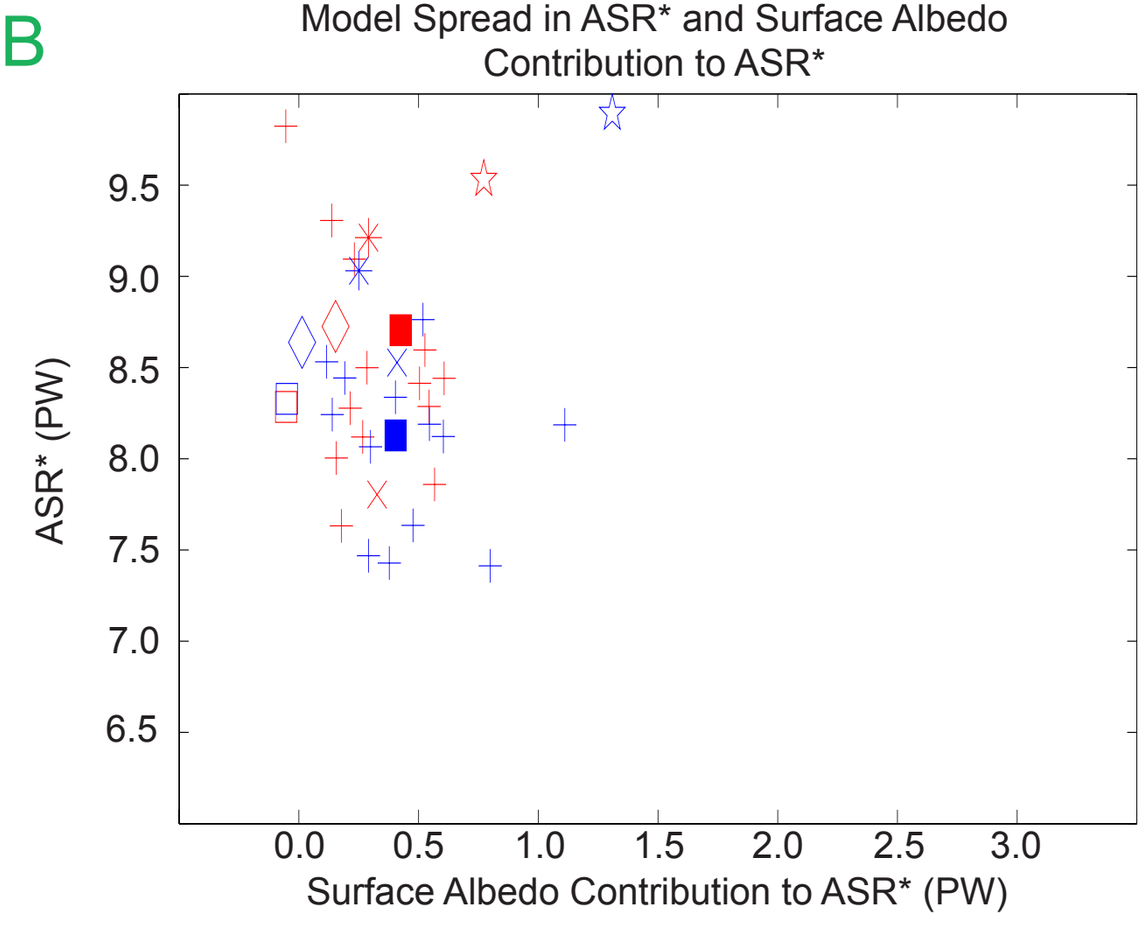

Figure 9. (a) ASR* versus atmospheric contribution to ASR* in each the NH and SH (blue and red plus signs) of the CMIP3 PI model ensemble, observations (filled squares), and additional model simulations. The theoretical prediction of "Model A", as discussed in the text, is given by the black line. (b) as in (a) except plotted against surface albedo contribution to ASR*.

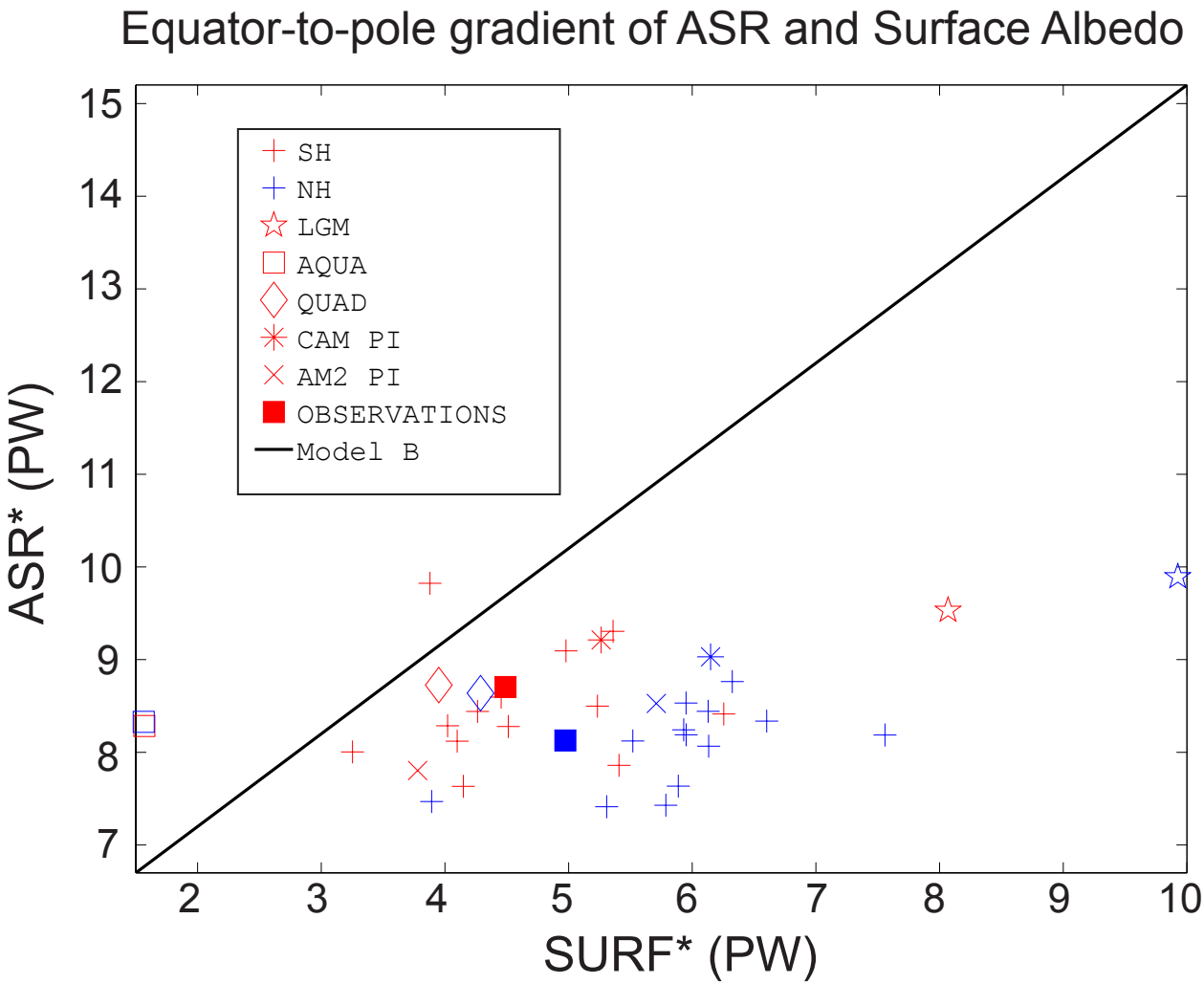

Figure 10. The equator-to-pole difference in ASR, ASR*, versus the equator-to-pole difference surface albedo, SURF*. The black line represents the prediction of "Model B" as discussed in the text.

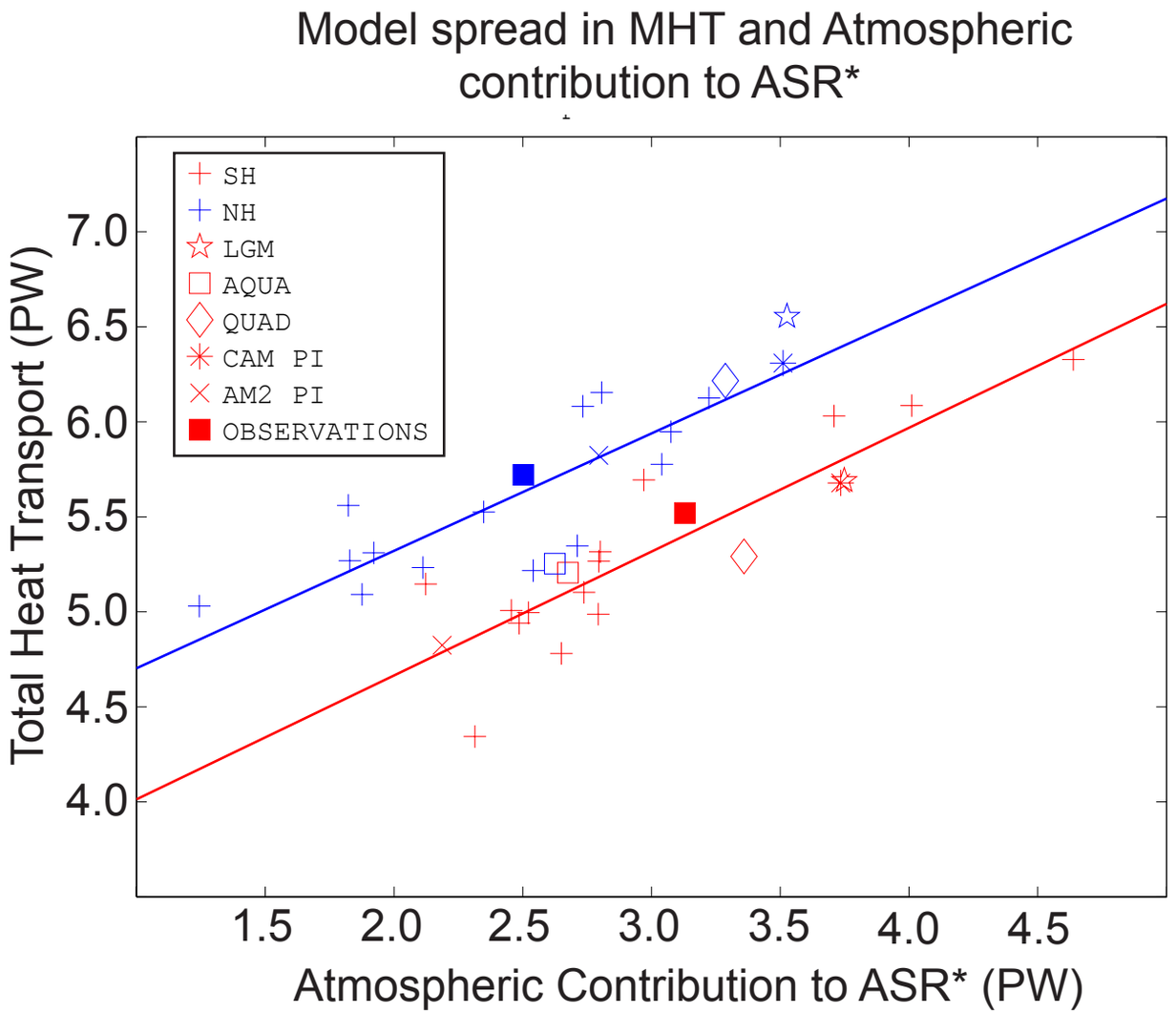

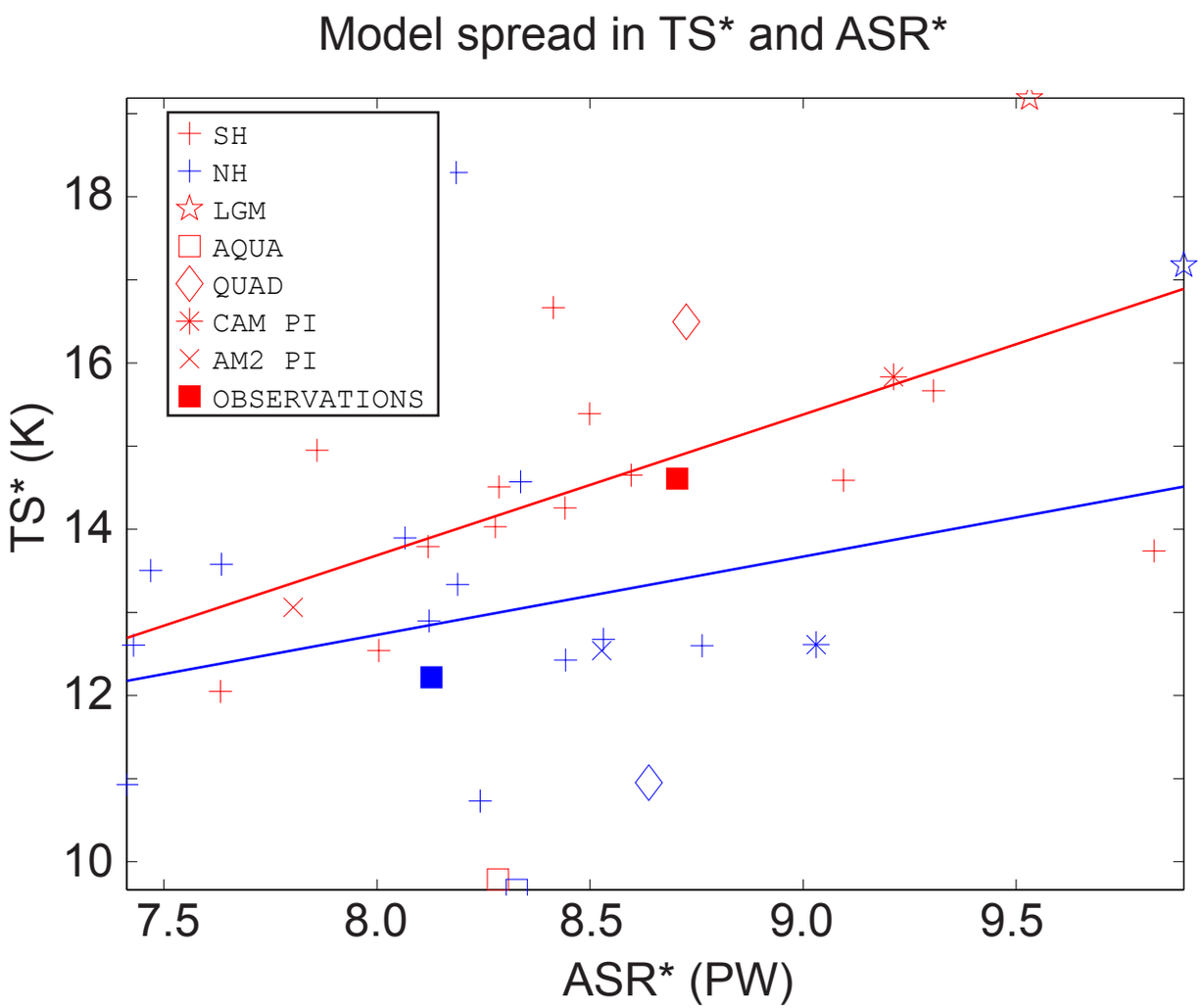

Figure 11. (a) MHT versus atmospheric contribution to ASR* in each hemisphere of the CMIP3 PI ensemble, observations, and additional model simulations. The blue (red) lines are the linear best fits to the PI model simulations in the NH (SH). (b) TS* versus ASR*.